ETS-guided iPSC-endothelial models recapitulate malaria pathogenesis

François Korbmacher[1], Hannah Fleckenstein[1,2], Rory Long[1,3], Patryk Poliński[1], Livia Piatti[1], Borja López-Gutiérrez[1], Alina Batzilla[1,3], Dennis Crusius[1], Vikas Trivedi[1,4], Miki Ebisuya[1,4,5]*, Maria Bernabeu[1*#]

[1]European Molecular Biology Laboratory (EMBL) Barcelona, Barcelona, Spain

[2]European Molecular Biology Laboratory (EMBL), Cell Biology and Biophysics Unit, Heidelberg, Germany

[3]Collaboration for joint PhD degree between EMBL and Heidelberg University, Faculty of Biosciences, Heidelberg, Germany

[4]Developmental Biology, EMBL Heidelberg, Heidelberg 69117, Germany

[5]Cluster of Excellence Physics of Life, TU Dresden, Dresden, Germany

[6]Max Planck Institute of Molecular Cell Biology and Genetics, Dresden, Germany

*Corresponding authors: maria.bernabeu@embl.es, miki.ebisuya@tu-dresden.de

[#]Lead Contact: maria.bernabeu@embl.es

Short title. ETS iPSC-models for malaria pathogenesis

Abstract

The sequestration of the malaria parasite *Plasmodium falciparum* in the microvasculature is a major driver of severe malaria, but its pathogenic mechanisms still remain unknown. Advancements in induced pluripotent stem cell (iPSC) technologies offer unique opportunities to study parasite interactions with blood vessels in a well-defined host environment. However, endothelial iPSC-differentiation methods often result in cells with mixed epithelial identity. Here, we have generated an iPSC line with inducible and simultaneous expression of ETS transcription factors (ETV2, FLI1, ERG), which resulted in improved endothelial cell identity and strong barrier function. These cells display a high affinity to infected red blood cells. Exposure to parasite products caused significant endothelial metabolic changes and splicing alterations. Furthermore, it disrupted the iPSC-endothelial barrier, as a consequence of transcriptional downregulation of key barrier processes, and alteration of severe malaria biomarkers. Our novel iPSC-based approach represents a new *in vitro* platform to study the pathogenesis of vascular infections.

Introduction

Plasmodium falciparum is the most severe human malaria parasite, causing over 600,000 deaths annually (*1*). Severe malaria affects multiple organs, including the lungs, kidneys, liver, heart, and brain, with cerebral malaria being one of the most fatal complications. A major contributor to organ pathogenesis is *P. falciparum*-infected red blood cell (infected RBC) accumulation in the microvasculature, a phenomenon also known as sequestration. Models of severe malaria comprise either *in vitro* or rodent malaria infection models, with the latter poorly recapitulating high levels of parasite sequestration reported in patients. Since the endothelium is the key interface for pathogenic interactions, most *in vitro* experimental approaches have focused on endothelial cells. Unfortunately, immortalised cell lines often lack crucial junctional markers, while primary cells are prone to rapid dedifferentiation and batch-to-batch variability (*2*). Moreover, both choices present poor endothelial barrier function, a critical feature for understanding vascular pathogenesis in severe malaria.

Induced pluripotent stem cells (iPSCs) have become a promising alternative to address these shortcomings. Differentiation methods have been widely used in malaria research to generate RBC from hematopoietic stem cells (*3, 4*). More recently, iPSC-derived erythrocytes have emerged as a novel tool for studying *P. falciparum* invasion into RBC (*5*), a technology that could be extended to dissect host-parasite interactions with blood vessels. One of the most commonly used endothelial differentiation methods generates iPSC-derived brain microvascular endothelial cell-*like* cells (iBMEC-*like*). This differentiation method has been popular, as it is easy to implement and yields cells with consistent and strong barrier properties, functionally mimicking those found at the blood-brain barrier (BBB) (*6, 7*). However, iBMEC-*like* cells have recently sparked controversy, particularly with regard to their endothelial identity, as they express epithelial markers (*8*). Nevertheless, iBMEC-*like* cells continue to be used in various applications (*9-11*), including the first iPSC *in vitro* model of cerebral malaria (*12*).

Lentiviral expression of ETS transcription factors has been proposed as a strategy to rescue the endothelial phenotype of iBMEC-*like* cells (*8*), and their overexpression is recently becoming a popular methodology for iPSC differentiation (*13-17*). Among ETS

62 transcription factors, ETV2, ERG, and FLI1 are regulators of endothelial development.
63 ETV2 stands out as a key orchestrator, coordinating the development by activating
64 specific endothelial gene expression and even enabling the direct conversion of somatic
65 cells into endothelial cells (*8, 18, 19*). ERG and FLI1 are both described as essential
66 factors in endothelial development, angiogenesis, and maintenance (*20, 21*). However,
67 to date, differentiation systems that promote ETS transcription factor overexpression have
68 not been applied to investigate malaria pathogenesis, neither via lentiviral transduction
69 nor through the introduction of stable transgenes. Here, we generated a doxycycline-
70 inducible, stable transgenic iPSC line that upregulates ETV2, ERG, and FLI1 during
71 iBMEC endothelial differentiation. The resulting cell type, ETS-iBMEC, presented
72 increased transcription of endothelial markers and downregulation of epithelial
73 transcripts. Although ETS-iBMECs showed equally strong barrier properties as iBMEC-
74 *like* cells when grown in a 3D model, they exhibited a marked shift towards endothelial
75 ultrastructural morphology. Perfusion of *P. falciparum*-infected RBCs displayed increased
76 cytoadhesion to ETS-iBMECs, and parasite products induced endothelial barrier
77 disruption, two key pathogenic hallmarks of severe and cerebral malaria. Moreover,
78 incubation with parasite egress product induced a progressive transcriptional
79 dysregulation of endothelial development genes, robust downregulation of junctional,
80 cytoskeletal, and basement membrane anchor genes in ETS-iBMECs. Interestingly, we
81 also observed a dysregulation of spliceosome and metabolic pathways, revealing
82 potential additional mechanisms for endothelial disruption.

83

84 **Results**

85 **ETS transcription factors promote endothelial differentiation in a DOX-inducible**
86 **iPSC line**

87 We developed an endothelial differentiation protocol based on the widely used iBMEC-
88 *like* protocol, including the addition of hypoxia, which has been shown to improve barrier
89 functionality (Fig. 1) (*7, 22*). To boost the endothelial identity of iBMEC-*like* cells, we
90 genetically engineered the iPSC(IMR90-4) line with a doxycycline (DOX)-inducible Tet-
91 One system to overexpress ETV2, ERG, and FLI1 (ETS) transcription factors (Fig. 1A).

92 This was achieved through a piggyBac transposase, which facilitated genomic integration
93 of the three inducible ETS factors (Fig. S1A). A clone exhibiting robust induction of all
94 three factors was selected (Fig. S1B). Differentiation of the DOX-induced cells (hereafter
95 referred to as ETS-iBMECs) was performed using the standard iBMEC-*like* protocol, with
96 DOX-induction of ETV2, ERG, and FLI1 from day 6 to day 11 (Fig. 1B), during the
97 endothelial expansion phase (*7, 8*). To rule out silencing of the Tet-One system over the
98 course of differentiation, we generated a parallel DOX-inducible iPSC line expressing
99 fluorescent reporters. Fluorescence imaging confirmed stable signal intensity throughout
100 the differentiation timeline, validating the robustness of the DOX-induction system (Fig.
101 S1C).

102 To fully assess the robustness of the ETS-driven differentiation, we characterised the
103 endothelial identity of the DOX-induced cells (ETS-iBMECs) and benchmarked it against
104 the non-induced control (iBMEC-*like*) (Fig. 1B) using immunofluorescence,
105 transcriptomics, barrier functional assays, and electron microscopy. Immunofluorescence
106 assays showed a consistent loss of epithelial EPCAM over the course of DOX induction,
107 being absent at day 11. Conversely, the expression of the endothelial marker CD31 was
108 significantly increased at day 11 in ETS-iBMECs (Fig. 1C). Furthermore, labelling of the
109 tight junction marker ZO-1 and adherens junction protein β-Catenin revealed notable
110 changes in cell morphology, with DOX-induced cells becoming smaller and elongated
111 after ETS induction (Fig. 1D). Moreover, the ETS-induced cells responded to TNFα
112 endothelial activation by increasing the expression of ICAM1, a key endothelial receptor
113 responsible for recruitment of *P. falciparum*-infected RBCs and leukocytes (*23*). Similarly,
114 the thrombin receptor PAR1, associated with severe malaria through dysregulation of
115 EPCR (*24*), displayed increased expression following DOX-induction (Fig. 1E). Together,
116 these results show that the ETS-induced stable iPSC line promotes a shift towards
117 endothelial identity, while non-induced iBMEC-*like* cells retain features reminiscent of
118 epithelial cells.

119

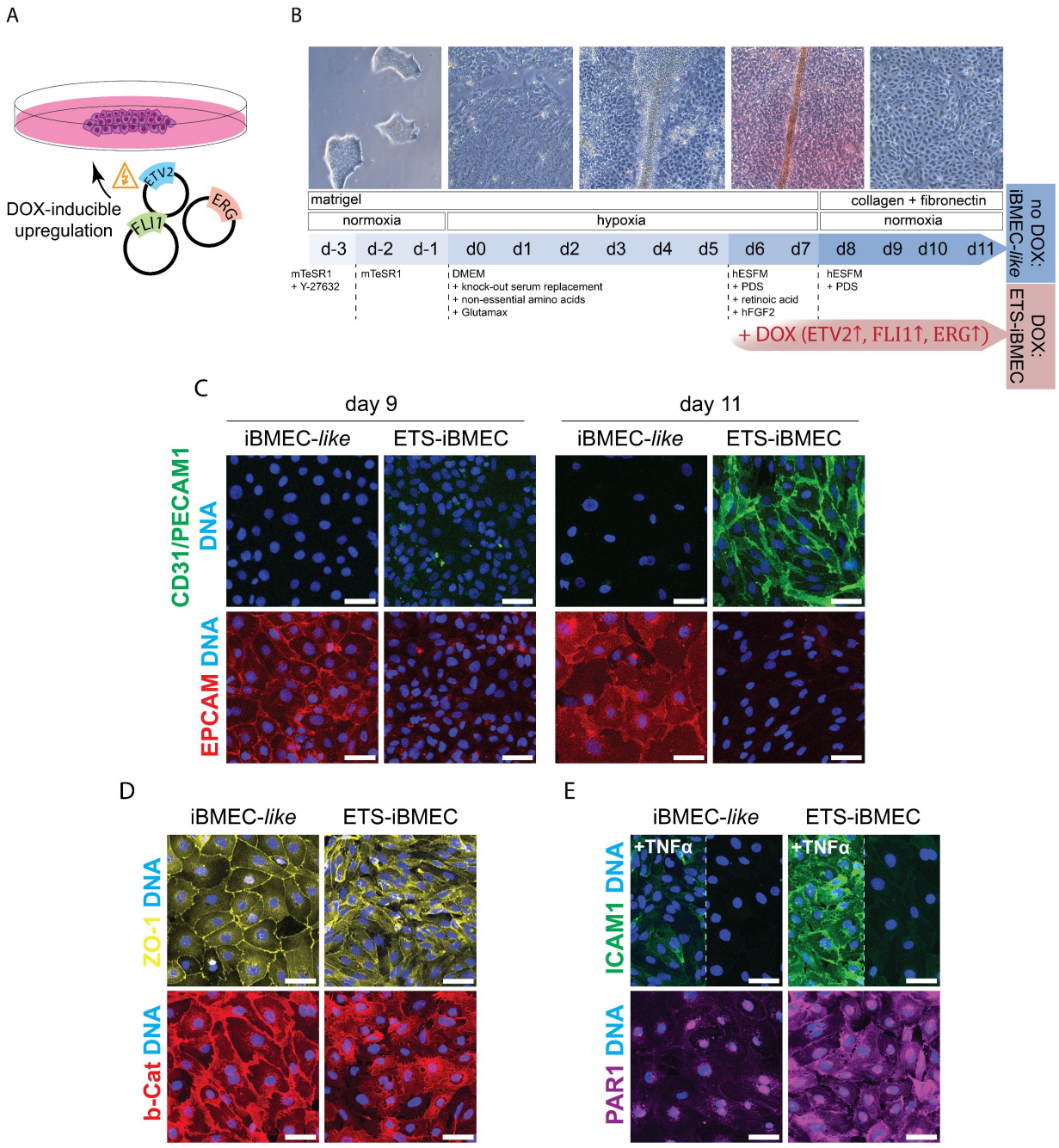

Fig. 1 – **Generation of the ETS-iBMECs** (**A**) The stable transgenic line was generated by transfecting iPSCs with a DOX-inducible upregulation system for the ETS-transcription factors: ETV2, ERG, and FLI1. (**B**) During the iBMEC-*like* differentiation protocol, the ETS-transcription factors were DOX-induced from day 6 until day 11 to generate ETS-iBMECs. A schematic representation of the iBMEC-*like* differentiation is shown above. (**C**) Immunofluorescence confocal microscopy of ETS-iBMEC and iBMEC-*like* cells stained with antibodies against epithelial EPCAM (red), endothelial CD31/PECAM1 (green), and nuclei (blue; DAPI) in samples fixed at day 9 and day 11 after differentiation. (**D**) Immunofluorescence confocal imaging of ETS-iBMEC and iBMEC-*like* cells with

antibodies against tight junction protein ZO-1 (yellow), and adherens junction protein β-catenin (red). (**E**) Immunofluorescence staining of the endothelial receptor ICAM1 (green), with and without prior TNFα stimulation, and the thrombin receptor PAR1 (purple) and nuclei (blue, DAPI). Scale bars, 100 µm.

ETS-iBMECs present increased expression of endothelial transcripts

To dissect the transcriptional changes triggered by ETV2, ERG and FLI1 upregulation, we performed bulk RNA sequencing (RNA-seq) and compared the expression profiles of ETS-iBMECs with their non-induced counterpart and primary brain microvascular endothelial cells (primary brain ECs). Differential gene expression analysis confirmed the overexpression of ETV2, ERG, and FLI1, and revealed that ETS-iBMECs upregulate genes associated with endothelial identity (*CDH5, PECAM1, FLT1, FLT4, TIE1*), as well as genes involved in angiogenesis and vascular development (*ANGPT2, TEK, ENG, APLN, ROBO4, EGFL7, SCUBE1, VASH1, RASIP1*), together with the vascular tight junction transcript *CLDN5*. Conversely, many epithelial genes were found to be downregulated (*CDH3, ELF3, EPCAM, ESRP1, GRHL2, OVOL1, OVOL2, TP63*) (Fig. S2), highlighting a clear transcriptional divergence between ETS-iBMEC and iBMEC-*like* cells. Gene ontology (GO) over-representation analysis further supports the shift towards an improved endothelial identity, highlighting biological processes involved in angiogenesis, endothelial proliferation, blood circulation, and cell adhesion being upregulated in ETS-iBMEC (Table S1). Indeed, the top five most significantly upregulated biological terms include angiogenic, circulatory, and vascular developmental processes, reflecting a strong shift toward endothelial programming after ETS induction (Fig. 2A). Additional upregulated clusters included pathways involved in signal transduction and cellular homeostasis, such as G-protein coupled pathways, ion transport, and tissue homeostasis, alongside cell physiological processes related to chemotaxis and migration, cell adhesion, and synaptic organization (Fig. 2B). Notably, the synaptic organisation cluster includes several genes expressed by endothelial cells, such as *NRP1*, *NRP2*, *PLXND1*, *RELN*, and *NLGN2,* that are key regulators of angiogenesis and neurovascular interactions (Table S1). DOX induction also enhanced the expression of genes involved in immune activation, highlighting the potential of ETS-iBMECs as an *in vitro* platform for

modelling inflammatory responses, a relevant feature for infection models. Conversely, mainly non-endothelial morphogenetic processes were downregulated, including meso- and ectodermal developmental processes of epidermis, skin, glands, bones and muscle tissue as the most significant decreased processes (Fig. 2C). Among these, epithelial developmental processes were found to be downregulated, together with terms associated with cell-contact organisation, extracellular organisation, cell motility, and multicellular organisation (Fig. 2D).

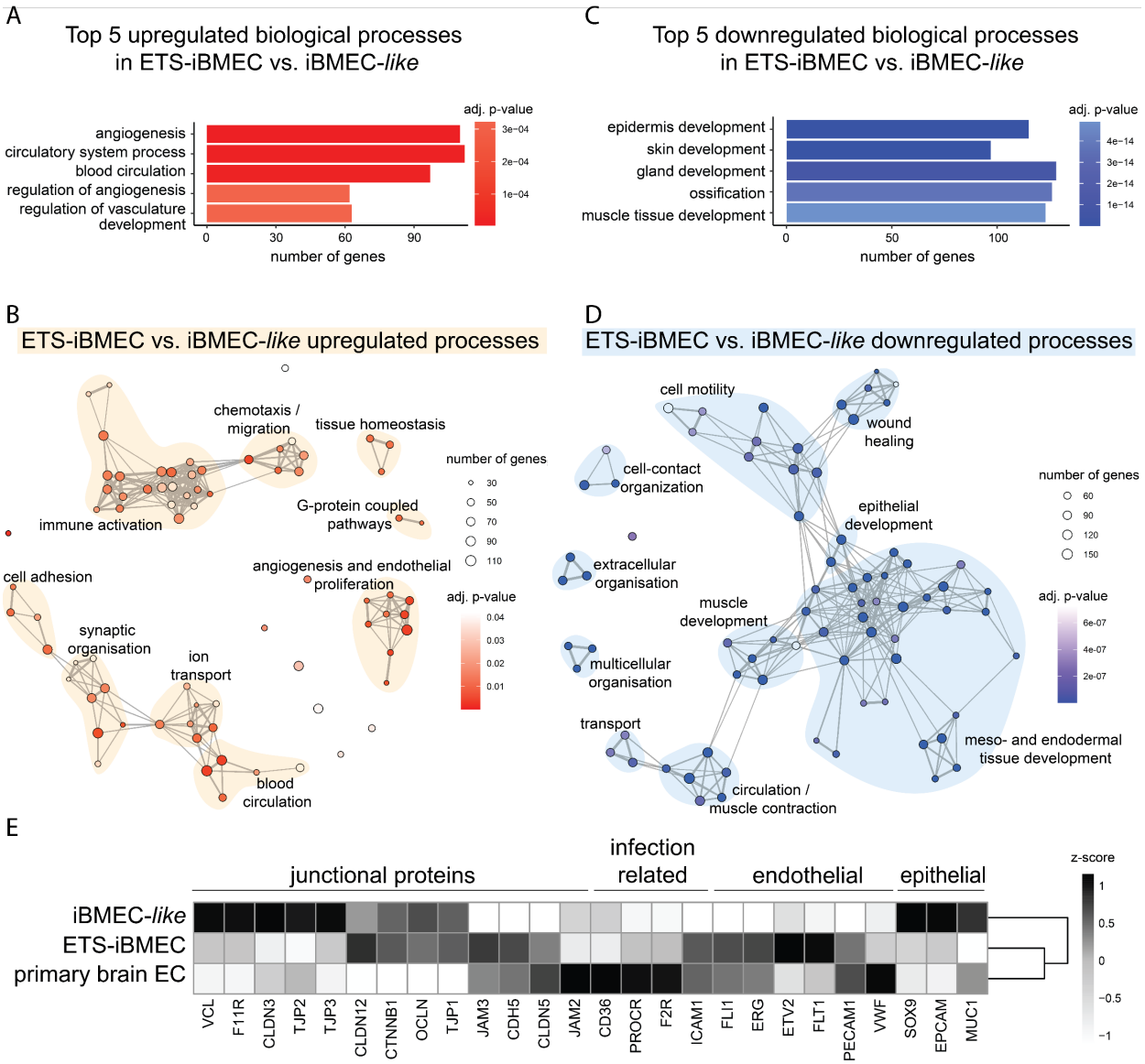

Fig. 2 – Transcriptional analysis of bulk RNA-seq in ETS-iBMECs (DOX), iBMEC-*like* (no DOX) and primary brain ECs. (**A**) Top 5 significantly upregulated GO biological processes and (**B**) GO term over-representation analysis map of differentially upregulated

genes on ETS-iBMEC compared with iBMEC-*like*. (**C**) Top 5 significantly downregulated GO biological processes and (**D**) GO term over-representation analysis map for differentially downregulated genes on ETS-iBMEC compared with iBMEC-*like*. The GO term maps show the 75 most significant GO term over-representation analyses from biological processes, which include ≥ 30 differentially expressed genes with adjusted p-value < 0.05 and $\log_2$FC > ±1. Node connections indicate shared genes, and node clusters are manually annotated. (**E**) Normalised gene expression of a selection of endothelial and epithelial genes across iBMEC-*like* cells, ETS-iBMEC and primary brain endothelial cells (primary brain EC). Z-score scaled by column (gene).

To further compare the expression profiles of the induced cell line with primary brain ECs, a widely used model for malaria studies, we analysed a curated panel of key endothelial and epithelial genes, along with markers important for modelling severe malaria pathogenesis (Fig. 2E). This analysis revealed a similar expression of these markers in ETS-iBMECs and primary brain ECs compared to iBMEC-*like* cells. ETS-iBMECs and primary brain ECs both exhibited similar expression levels of the endothelial marker *PECAM-1* (CD31) and did not express epithelial genes such as *MUC1*, *EPCAM* and *SOX9*. Endothelial transcription factors *ERG* and *FLI1* reached comparable levels of expression in both primary brain ECs and ETS-iBMECs. However, ETV2 was expressed at higher levels in DOX-induced cells compared to primary brain ECs, an expected phenotype due to the downregulation of ETV2 in fully differentiated endothelial cells. Analysis of junctional proteins showed that DOX-induced ETS-iBMECs partially recapitulate the expression profile of primary brain ECs. Junctional genes like *CLDN5* (Claudin-5), *CDH5* (VE-Cadherin), and *JAM3* showed similar expression in both ETS-iBMECs and primary brain ECs, while other important endothelial tight junctional genes like *TJP1* (ZO-1), and *OCLN* (Occludin) showed a higher expression in ETS-iBMECs, suggesting an improvement in endothelial barrier properties in DOX-induced cells. Lastly, parasite-interacting receptors such as *PROCR* (EPCR) and *ICAM1* show increased expression following DOX induction, except for *CD36*. Together, these transcriptional changes highlight a broad transcriptional shift in ETS-iBMECs, with an expression pattern that more closely resembles primary brain ECs (Fig. 2E).

204 **ETS-iBMEC microvessels lose epithelial ultrastructural features while maintaining**
205 **barrier function**

206 To assess the microvascular properties of ETS-iBMECs, we incorporated them into a
207 previously established 3D microfluidic device consisting of a pre-patterned type I collagen
208 hydrogel, generated through soft lithography and injection moulding (*25*). Primary human
209 astrocytes (HA) and brain vascular pericytes (HBVPs) were seeded at a 7:3 ratio in the
210 collagen bulk (*26*), while endothelial cells were seeded into the microfluidic network by
211 gravity-driven perfusion (Fig. 3A). After a few days in culture, the endothelial cells formed
212 perfusable microvessels with sparse contacts to the surrounding glial and perivascular
213 cells. Both iBMEC-*like* cells and ETS-iBMECs formed perfusable microvessels in this
214 setup (Fig. 3B). Nevertheless, seeding required a pre-coating with fibronectin and
215 collagen IV and was more challenging than with primary brain ECs, resulting in much
216 lower throughput. To determine barrier function, we measured the apparent trans-
217 endothelial permeability following perfusion with 40 kDa and 10 kDa dextran (Fig. 3C).
218 Remarkably, ETS-iBMEC microvessels reached permeability values of $<10^{-8}$ cm/s with
219 median levels of 1.5×10^{-8} cm/s, representing an over 100-fold barrier improvement over
220 primary brain EC microvessels that present median permeability values of 4.3×10^{-6} cm/s
221 in the same setup. Furthermore, both iBMEC-*like* and ETS-iBMEC microvessels were
222 largely impermeable to smaller molecular weight tracers (Fig. 3D-E, Fig. S3A), with ETS-
223 iBMECs showing slightly elevated 10 kDa dextran permeability rates (median 5.9×10^{-8}
224 cm/s) compared to iBMEC-*like* controls (median 8.8×10^{-9} cm/s). These results
225 demonstrate that microvessels made from iBMEC-*like* and ETS-iBMECs possess
226 stronger barrier properties than those derived from primary brain ECs.

227 While both differentiated cell types exhibit robust barriers, their transcriptional profiles are
228 markedly distinct. To better understand these differences, we conducted transmission
229 electron microscopy (TEM) on thin sections of the 3D brain microvascular model. IBMEC-
230 *like* cells showed greater apical-basal height, forming elongated junctions characterized
231 by the typical architecture of epithelial junctional complexes: apical tight junctions followed
232 by adherens junctions, prominent desmosomes, and interdigitated regions (Fig. 3F, G).
233 Conversely, ETS-iBMECs were flatter and had shorter junctions (Fig. 3F), containing tight

junctions, and no desmosomes were observed (Fig. 3G). Additionally, the two cell types exhibited distinct apical surface morphologies: iBMEC-*like* cells displayed epithelial microvilli-like projections, which were rarely observed in ETS-iBMECs (Fig. 3H). The ultrastructural morphology of ETS-iBMECs closely resembled that of primary brain ECs (*27*) (Fig. S3B), further suggesting a loss of epithelial characteristics. Altogether, these findings demonstrate that ETS-iBMECs outperform primary brain ECs in barrier function, while displaying enhanced endothelial transcription and ultrastructure compared to iBMEC-*like* cells.

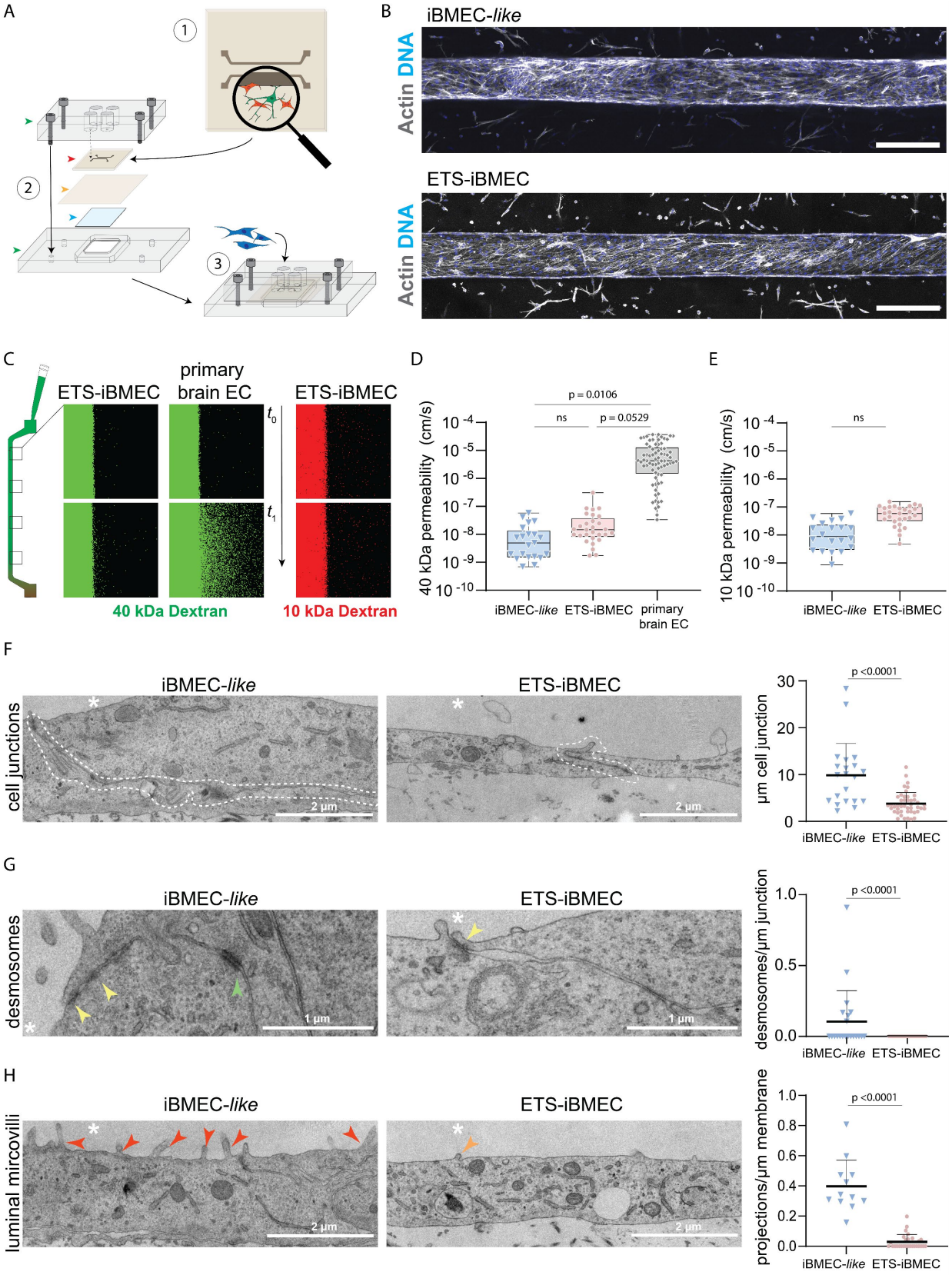
A
1
2
3
B
iBMEC-like
Actin DNA
ETS-iBMEC
Actin DNA
C
ETS-iBMEC
primary brain EC
ETS-iBMEC
t_0
t_1
40 kDa Dextran
10 kDa Dextran
D
p = 0.0106
ns
p = 0.0529
40 kDa permeability (cm/s)
iBMEC-like
ETS-iBMEC
primary brain EC
E
ns
10 kDa permeability (cm/s)
iBMEC-like
ETS-iBMEC
F
iBMEC-like
ETS-iBMEC
cell junctions
2 µm
µm cell junction
p <0.0001
iBMEC-like
ETS-iBMEC
G
iBMEC-like
ETS-iBMEC
desmosomes
1 µm
desmosomes/µm junction
p <0.0001
iBMEC-like
ETS-iBMEC
H
iBMEC-like
ETS-iBMEC
luminal mircovilli
2 µm
projections/µm membrane
p <0.0001
iBMEC-like
ETS-iBMEC

242

Fig. 3 – Barrier and ultrastructural morphological characterisation of ETS-iBMEC (DOX) and iBMEC-*like* cells (no DOX). (**A**) Schematic of a 3D-engineered microfluidic device composed of a collagen hydrogel containing primary astrocytes (green cells) and pericytes (red cells). The upper collagen layer (red arrow) includes two pre-patterned, parallel microchannels (1), and is assembled with a flat lower collagen layer (yellow) and a coverslip (blue) between two polymeric jigs (green) (2). The top jig has inlet and outlet wells, which are aligned to the entry and exit of each microchannel, allowing for direct perfusion. ETS-iBMECs, iBMEC-*like* and primary brain ECs are seeded along the microchannel by luminal gravity perfusion through the inlet (3). (**B**) The endothelial cells generate tubular microvessels. Top: iBMEC-*like* microvessels, bottom: ETS-iBMEC microvessels both stained for actin (phalloidin, grey) and DNA (DAPI, blue). Scale bar: 100 µm. (**C**) Representative images of barrier permeability assay on 3D microvessels perfused with fluorescently labelled 40 kDa FITC dextran (green) and 10 kDa AF647 dextran (red). Analysis was done in squared regions of interest (ROI) along iBMEC-*like*, ETS-iBMEC and primary brain EC microvessels at two different timepoints of perfusion (t_1 = 150 seconds). (**D**, **E**) Quantified apparent permeability to 40 kDa dextran and 10 kDa dextran. Each dot represents individual ROIs in iBMEC-*like* (N = 3 microvessels), ETS-iBMECs (N = 4 microvessels) and primary brain ECs (N = 8 microvessels). Statistical analysis performed with Dunn's multiple comparisons test. Boxplots indicate median and interquartile range (**F** to **H**). TEM images of iBMEC-*like* and ETS-iBMEC microvessels. Scale bars: 2 µm. (**F**) Representative images of junctions outlined with a white dotted line (left and center), and quantification of differences in junctional length (right). Statistical significance calculated by Mann-Whitney U test. iBMEC-*like* (N = 21 junctions), and ETS-iBMEC (N = 45 junctions). (**G**) Representative images of tight junctions (yellow arrows), characterised by tightly connected electron-dense membranes, and desmosomes with electron-dense plaque and wider intermembrane space (green arrow). Statistical significance of the presence of desmosomes calculated by Mann-Whitney U test. iBMEC-*like* (N = 21 junctions), ETS-iBMEC (N = 45 junctions). (**H**) Representative images of microvilli (red arrow) and smaller projections (orange arrow). Statistical difference in the quantification of all projections calculated by Mann-Whitney U test. iBMEC-*like* (N = 28 ROIs) and ETS-iBMEC (N = 12 ROIs).

P. falciparum presents strong binding to ETS-iBMECs under flow

Cytoadhesion of parasite-infected RBCs to endothelial EPCR and ICAM1 is a key determinant of severe and cerebral malaria (*28-32*). To evaluate the suitability of ETS-iBMECs for malaria *in vitro* pathogenesis studies, we first tested their capacity to bind *P. falciparum*-infected RBCs. Fluorescently labelled *P. falciparum*-infected RBCs were perfused for 30 minutes through microfluidic flow chambers seeded with either iBMEC-*like*, ETS-iBMEC, or primary brain ECs (Fig. 4A). Unbound parasites were washed out

for 10 minutes and bound parasites were quantified after fixation. The *P. falciparum* line ITGICAM1 is known for its dual binding to CD36 and ICAM1 (Fig. S4, 4B), and showed significantly higher adhesion to ETS-iBMECs compared to iBMEC-*like* cells, and a non-significant increase in binding relative to primary brain ECs (Fig. 4C-D). The IT4var19 parasite line, known for strong affinity to endothelial EPCR (Fig. S4, 4B), a phenotype highly enriched in severe malaria patients, exhibited robust cytoadhesion to all three cell types (Fig. 4C-E). Notably, IT4var19 showed increased binding to ETS-iBMECs compared to iBMEC-*like* cells and primary brain ECs, although the difference was not statistically significant (Fig. 4E). Overall, the improved endothelial identity and the strong binding rates for *P. falciparum*-infected red blood cells exemplify the usefulness of ETS-iBMECs as an alternative cell model for malaria pathogenesis.

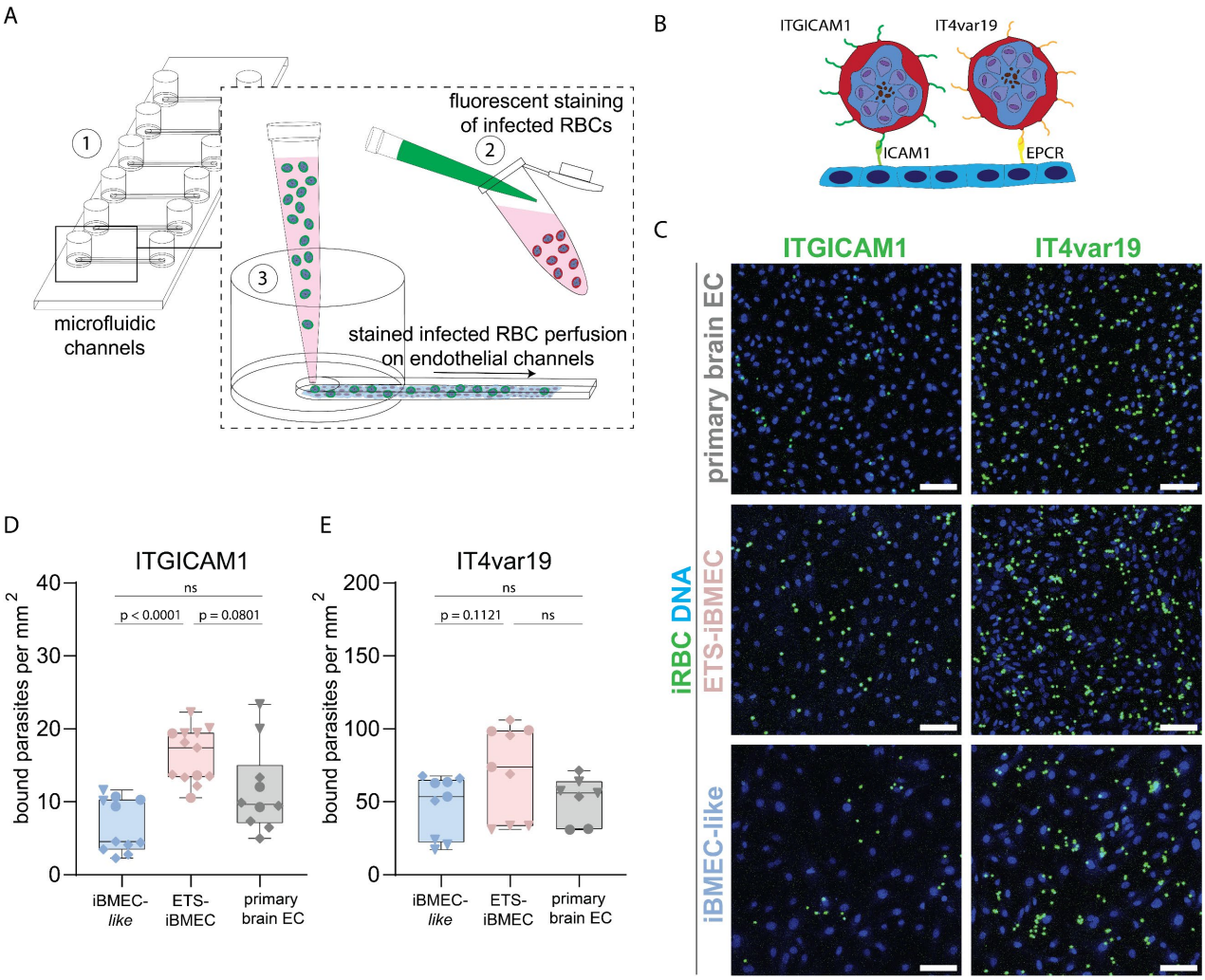

294 **Fig. 4 – *P. falciparum in vitro* infection modelling for parasite cytoadhesion.** (**A**)
295 Endothelial channels are formed in microfluidic slides previously seeded with iBMEC-*like*,
296 ETS-iBMEC and primary brain EC cells (1). Infected red blood cells (infected RBCs) are
297 purified and fluorescently stained (2) and gravity-perfused through the endothelial
298 channels, where they adhere under flow to endothelial cells (3). (**B**) PfEMP1 variants
299 ITGICAM1 binds to the endothelial surface receptor ICAM1 and IT4var19 to EPCR. (**C**)
300 Representative images of parasite cytoadhesion assay to iBMEC-*like*, ETS-iBMEC and
301 primary brain EC channels. Infected RBCs in green, endothelial nuclear stain in blue.
302 Scale bar: 100 µm. (**D**, **E**) Quantification of bound infected RBCs for *P. falciparum* lines
303 ITGICAM1 (**D**) and IT4var19 (**E**) in microfluidic iBMEC-*like*, ETS-iBMEC and primary brain
304 EC channels. Dot plot shows *P. falciparum*-infected RBC average binding to regions of
305 interest, normalised per area (mm^2), of three independent experiments including different
306 differentiations and independent parasite purifications. Boxplots indicate the median and
307 interquartile range. Statistical analysis performed with Dunn's multiple comparisons test.
308 Each dot corresponds to averaged binding across one microchannel.

309

310 ***P. falciparum* induces transcriptional changes in ETS-iBMECs, including metabolic**
311 **alterations and alternative splicing events**

312 Next, we aimed to identify endothelial disruptive mechanisms upon exposure to *P.*
313 *falciparum*-infected RBCs. Accumulation of infected RBCs in the microvasculature results
314 in the localised release of parasite-derived products near the endothelium at the late
315 stages (schizonts) of the blood stage cycle, an event previously characterised as highly
316 disruptive to barrier integrity in primary endothelial cells of various tissues (*26, 27, 33-35*).
317 Here, we generated a solution containing parasite egress products by arresting the
318 egress of highly synchronised late-stage *P. falciparum*-infected RBCs using the reversible
319 protein kinase G inhibitor, compound 2 (C2), followed by the simultaneous release of
320 parasite-derived products upon its removal (Fig. 5A). To understand the molecular
321 mechanisms upon exposure to *P. falciparum*-iRBC products, we performed bulk RNA-
322 seq after 8 and 24 hours of exposure to 5×10^7 egressed infected RBCs/ml. As a control,
323 we also sequenced iBMEC-*like* and primary brain ECs under the same conditions. While
324 most of the dysregulated transcripts were unique to each cell type, some commonalities
325 were observed between all three or in pairwise comparisons, suggesting that these
326 pathways are commonly disrupted by the malaria egress products (Fig. S5A-B).

327 Shared dysregulated GO term processes included upregulation of sterol and cholesterol
328 synthesis pathways (Fig. 5B, D, E, Fig. S5C). Other upregulated processes in ETS-

329 iBMEC included circulatory regulation and synaptic organisation, with the latter including
330 endothelial transporters important for barrier regulation (AMPAR, NMDAR, KAR, CACN)
331 and angiogenesis-related transcripts (*NTN1, SEMA3, SEMA4, SEMA7, L1CAM*) (Table
332 S2). A common downregulated process among the three cell types, with special
333 relevance in ETS-iBMEC, was RNA splicing (Fig. 5C), along with other terms associated
334 with RNA processes and translational regulation (Fig. 5C, Fig. S5C). Spliceosome
335 transcripts showed early decreased expression after 8 hours, sustained throughout the
336 24-hour experiment (Fig. 5F). Because alterations in pre-mRNA processing can result in
337 profound changes in the endothelial cell biology, we then focused our analysis on
338 alternative splicing after exposure to infected RBC products. Using vast-tools (*36*), we
339 identified 692 events (about 7%) that were differentially spliced between the two
340 conditions (more than 15% of a particular mRNA alternatively spliced; ΔPSI ≥ 15) (Table
341 S3). The most common events included alternative exon splicing (37.7%) and intron
342 retention (28.3%) (Fig. 5G). Based on data from VastDB, many of the detected events
343 are predicted to disrupt the open reading frame (51.3%) or create alternative protein
344 isoforms (30.7%) (Fig. 5H). Moreover, 112 events had substantial changes in splicing
345 (ΔPSI ≥ 25). Among them were proteins responsible for autophagy (ATG16L2, RB1CC,
346 SQSTM1), with important functions in cytoskeleton dynamics (Tropomyosin 1), and a
347 histone deacetylase regulating inflammatory gene expression (HDAC5/7/8) (Table S3).
348 These data suggest that infected RBC products cause profound changes in ETS-iBMEC
349 homeostasis, including alterations in transcription and/or potential changes in alternative
350 splicing.

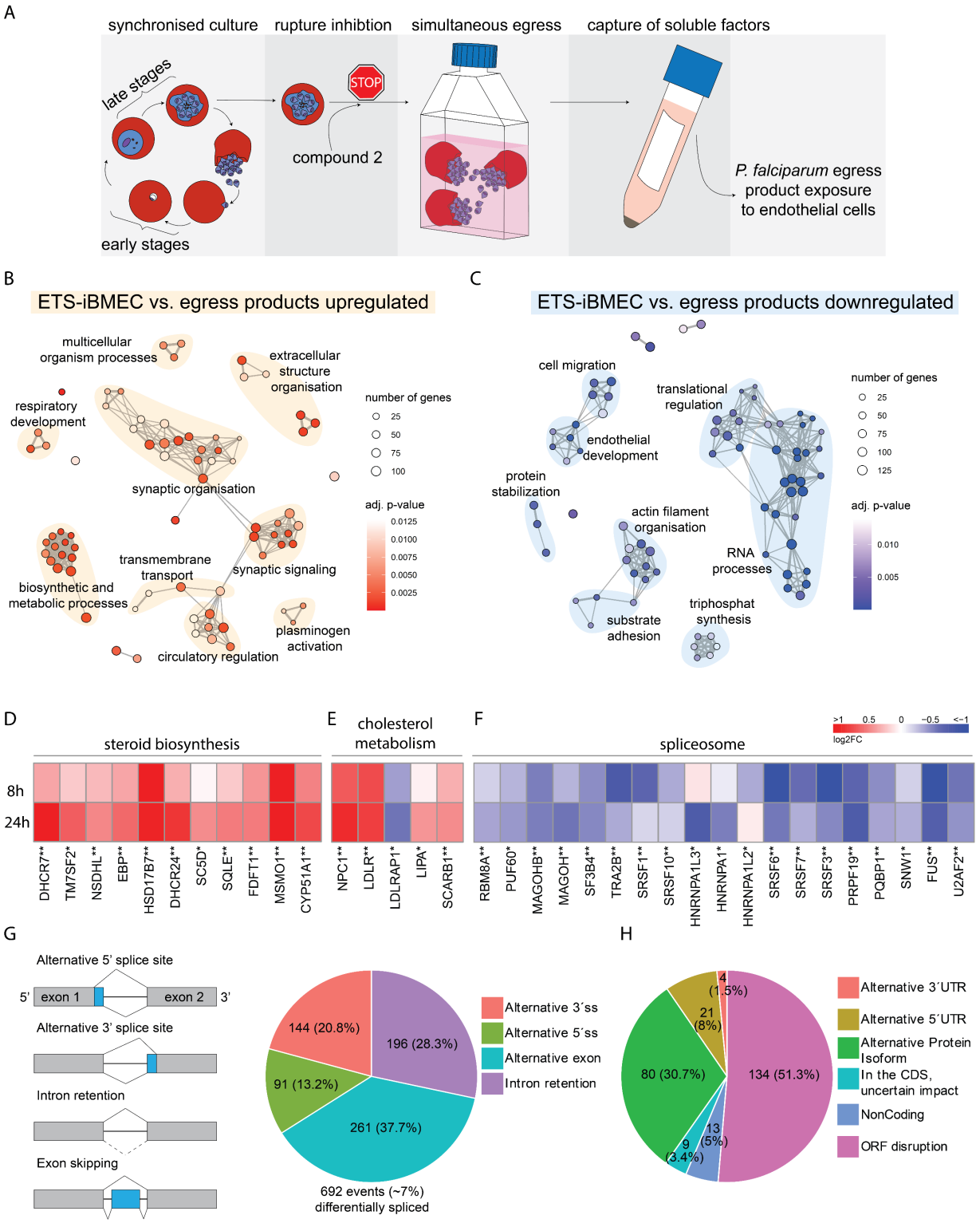

Fig. 5 – Transcriptional profiling of ETS-iBMEC response to malaria egress product exposure. (**A**) Schematic protocol of malaria egress media purification. Schizonts are purified from a synchronous asexual blood stage culture and exposed to compound 2, a schizont rupture inhibitor. After incubation, late schizonts are resuspended in endothelial

356 media for simultaneous rupture in defined concentrations. Soluble factors are purified by
357 centrifugation, and the resulting supernatant is used for downstream endothelial assays.
358 (**B and C**) GO term over-representation analysis of (**B**) upregulated and (**C**)
359 downregulated GO biological processes. Shown are the 75 most significant processes
360 (adjusted p-value < 0.05, $\log_2$FC > ± 0.1). Node connections indicate shared genes
361 between GO terms, and node clusters are manually annotated. (**D, E and F**) Heatmaps
362 display $\log_2$ fold changes after 8- and 24-hour egress product exposure compared to
363 media controls of key genes in (**D**) steroid biosynthesis pathways, (**E**) cholesterol
364 metabolism and (**F**) spliceosome pathways. Asterisks indicate significant DEseq2
365 expression (adjusted p-value < 0.05) for one (*) or both (**) time points. (**G**) Distribution
366 of alternatively spliced events by type. Plotted event numbers are differentially spliced
367 (ΔPSI ≥ 15) between the ETS-iBMEC basal condition and *P. falciparum*-infected RBC at
368 24h. Alternative 3'/5' ss, alternative splice-site acceptor/donor selection. (**H**) Predicted
369 impact of alternatively spliced events on the proteome based on data from VastDB. Many
370 of the events are predicted to disrupt ORFs (e.g., frameshift and/or premature termination
371 codon) or to generate alternative protein isoforms.
372

373 **_P. falciparum_-egress products disrupt the ETS-iBMEC barrier and alter the**
374 **transcription of endothelial junctional, cytoskeletal, and angiogenic pathways**

375 Endothelial barrier disruption plays an important role in severe malaria, especially in
376 complications such as cerebral malaria, characterised by severe brain swelling and blood-
377 brain barrier disruption (*37-39*). Multiple downregulated processes in the transcriptomic
378 analysis were suggestive of changes in barrier integrity, including cell migration, actin
379 organisation, substrate adhesion, and endothelial development (Fig. 5C). To determine
380 whether these changes would lead to endothelial barrier disruption in ETS-iBMECs, we
381 assessed trans-endothelial resistance through real-time impedance-based
382 measurements (xCELLigence). ETS-iBMECs were exposed to 1.25, 2.5, and 5×10^7
383 infected RBCs/mL—concentrations corresponding to the simultaneous egress of *P.*
384 *falciparum*-infected RBCs at parasitemias of 0.25%, 0.5%, and 1%, respectively (*37*). All
385 conditions tested led to a decrease in the cell index, indicative of compromised endothelial
386 integrity. Despite high variability, a plateau in endothelial breakdown was observed at
387 2.5×10^7 ruptured infected RBCs/mL (Fig. 6A, B). Overall, our results reveal that ETS-
388 iBMECs respond to the addition of *P. falciparum*-egress products through endothelial
389 barrier disruption.

390 A targeted transcriptomic analysis of endothelial junctional genes revealed a coordinated
391 and pronounced downregulation of adherens and tight junction markers, highlighting a
392 potential mechanistic axis of endothelial barrier destabilisation in response to malaria
393 products in ETS-iBMEC (Fig. 6C-D). Notably, key tight junction members, such as *CLDN5*
394 (Claudin-5), *F11R* (JAM-1), and *JAM3*, along with tight junction adaptors *TJP1* (ZO-1)
395 and TJP2 (ZO-2), were significantly downregulated, some early upon exposure and
396 others at later timepoints. Decreased expression of adherens junctional transcripts, *CDH5*
397 (VE-cadherin), *CTNNB1* (β-catenin), and *CTNNA1* (α-catenin), as well as other junctional
398 components such as *PECAM1* (CD31, Fig. 6G), was also found. In addition to the
399 decrease in cell-junction transcripts, *P. falciparum* egress products downregulate key
400 genes involved in actin dynamics. While actin isoforms (*ACTB, ACTG1*) remained stable,
401 components of the Arp2/3 complex (*ARPC2*, *ACTR2*, and *ACTR3*), involved in filament
402 branching, were downregulated early upon exposure (Fig. 6E). Furthermore, we observed
403 early (8h) and sustained (24h) transcriptional repression of most focal adhesion-
404 associated genes including *ZYK* (zyxin), *PXN* (paxillin), and *TLN* (talin), whereas others
405 such as *VCL* (vinculin) remained unchanged. Key regulators of focal adhesion formation
406 and stabilisation (ROCK1, ROCK2), along with late downregulation of integrins, were also
407 revealed. This occurred simultaneously to disruption in extracellular matrix secreted
408 proteins, including *COL4A1* and *COL4A2* downregulation and *LAMB1* upregulation (Fig.
409 6F). We also identified alterations in key vascular homeostatic and angiogenic processes,
410 including members of the VEGF pathway (*VEGFA*, *ROBO4*, *FLT1*, and *KDR),* Notch
411 signalling (*NOTCH1, NOTCH4*, *JAG2*, and *DLL4)*, and Angiopoietin/Tie axis (*ANGPT2*
412 and *TEK*) (Fig. 6G).

413 Notably, the downregulation of junctional, cytoskeletal and focal adhesion transcripts was
414 more pronounced and robust in ETS-iBMEC than in primary brain ECs (Fig. S6).
415 However, ETS-iBMEC did not show overexpression of viral processes and interferon
416 response, including the JAK-STAT pathway, a key pathogenic response predominantly
417 found in primary brain ECs in a 3D-blood brain barrier (*26*) (Fig. S5C). Nevertheless, we
418 identified additional important transcriptional dysregulations in primary endothelial cells
419 that have been recognised as biomarkers of clinical severe malaria (28). Of the selected
420 markers, seven showed significant upregulation at one or both time points, with the

strongest induction observed for ANGPTL4, STC2, ADM2, BDNF, and KISS1 (Fig. 6H). Overall, these results reveal that *P. falciparum*-infected RBC products profoundly affect vascular homeostatic pathways and highlight the use of ETS-iBMECs as a relevant model for malaria pathogenesis.

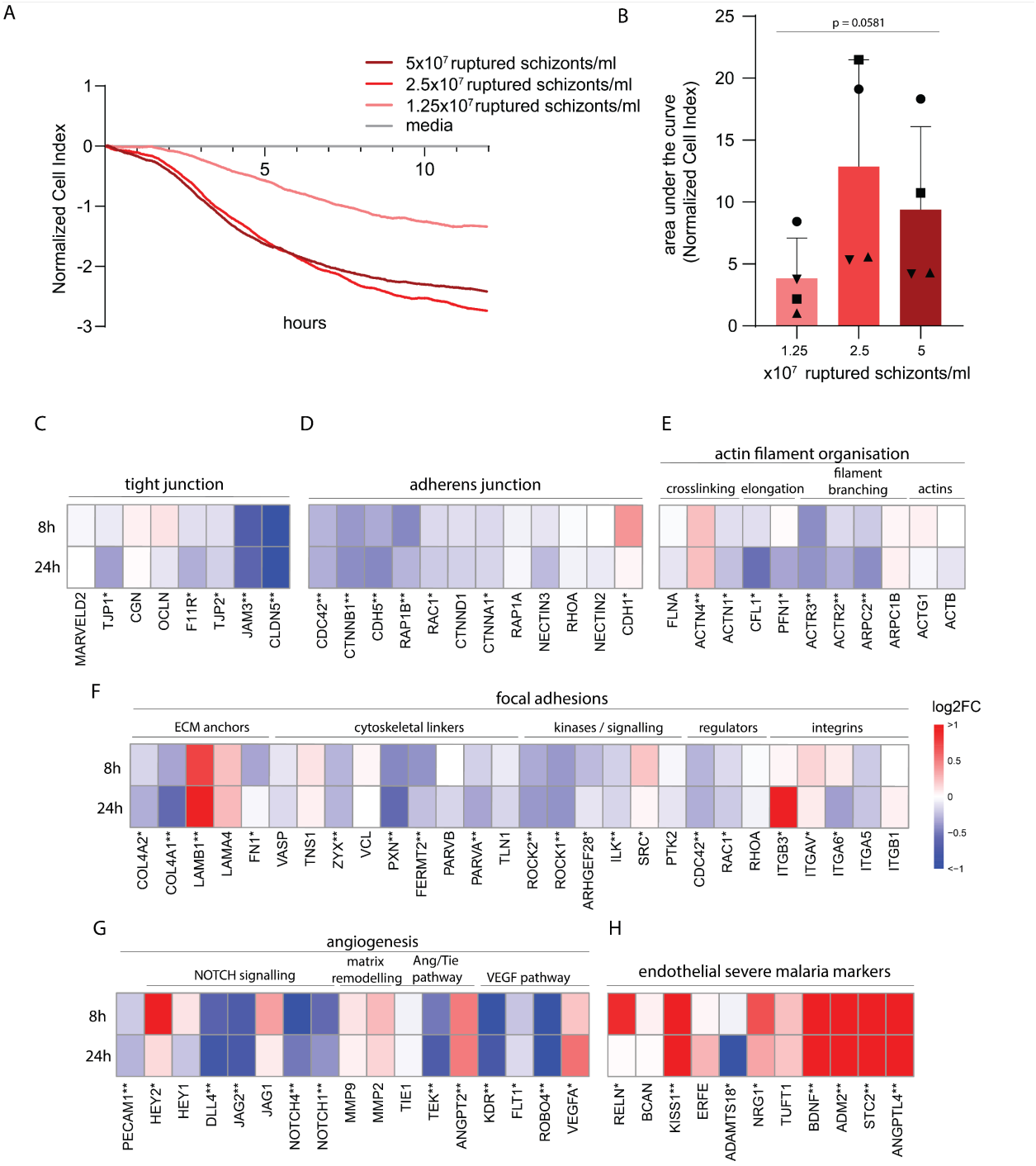

426 **Fig. 6 – Transcriptional changes induced by *P. falciparum* egress products in ETS-**
427 **iBMECs across barrier-associated gene categories**. (**A**) Representative record of
428 normalized cell index from real-time xCELLigence trans-endothelial impedance
429 measurements of ETS-iBMECs exposed to egress media in different concentrations. **(B)**
430 Resulting area under the curve analysis for 12 hours for four independent cell
431 preparations (one-way ANOVA). (**C-H**) Heatmaps display $\log_2$ fold changes after 8- and
432 24-hour egress product exposure, compared to media controls, for key genes involved in
433 the architecture of tight junctions (**C**), adherens junctions (**D**), actin filaments (**E**), focal
434 adhesions (**F**), a selection of key angiogenesis genes (**G**), and endothelial severe malaria
435 marker genes (**H**) (*40*). Asterisks indicate significant DESeq2 differential expression
436 (adjusted p-value < 0.05) for one (*) or both (**) time points.

437

438 **Discussion**

439 Research on severe malaria has been hampered by the lack of an animal model that
440 recapitulates the accumulation of *P. falciparum*-infected RBC in the brain
441 microvasculature. As an alternative, most *in vitro* pathogenesis models have used
442 immortalised or primary cells, which present inherent limitations such as loss of cell
443 identity and batch-to-batch variability (*26, 27, 34, 41-43*). The use of iPSC-differentiated
444 endothelial models for malaria research emerges as a promising alternative, allowing the
445 future development of patient-specific isogenic models. Although iPSC-based models
446 have recently been applied to model cerebral malaria (*12*), challenges to faithfully
447 recapitulate endothelial identity remain the main limitation in the stem cell bioengineering
448 field (*8*). Here, we have generated a stable iPSC transgenic line that directs endothelial
449 differentiation of iBMECs through DOX-induction of three key ETS transcription factors:
450 ETV2, ERG, and FLI1. We confirmed ETS-iBMECs as a valid model to study malaria
451 pathogenesis through binding studies by perfusing *P. falciparum*-infected RBCs under
452 flow, as well as transcriptomics. The newly developed models reveal that ETS-iBMECs
453 form elevated trans-endothelial barriers that are susceptible to breakdown upon exposure
454 to parasite products, and are associated with downregulation of tight and adherens
455 junctional markers, focal adhesion, and cytoskeletal markers, along with numerous
456 differential splicing events.

457 The essential role of ETS transcription factors in endothelial development is well
458 established (*8, 13, 15, 17, 44-47*), among which ETV2 particularly drives the emergence

459 of vasculogenic, generic endothelial cells (*48, 49*). Overexpression of ETV2 has been
460 widely used to promote endothelial differentiation, including electroporation (*13*), lentiviral
461 transduction (*8, 15-17*) or more recently with the generation of stable lines through
462 piggyBac-mediated integration (*45-48, 50, 51*). Our study, to our knowledge, is the first to
463 use a stable, transgenic iPSC line enabling inducible upregulation of three ETS-factors,
464 thereby robustly promoting endothelial identity. Consistent with previous studies (*8, 13,*
465 *15, 17, 44-48*), DOX induction in ETS-iBMECs strongly directed the differentiation toward
466 the endothelial lineage, as shown by increased expression of endothelial markers and
467 ultrastructural morphology, while maintaining enhanced brain-*like* barrier function. Our
468 approach not only streamlines experimental procedures but also allows for the selection
469 of a cell line with three stably integrated inducible transcription factors, including ETV2,
470 to further promote endothelial differentiation.

471 Although ETS-induction is not intended to generate brain-specific endothelial cells, ETS-
472 iBMECs markedly outperformed primary brain ECs in terms of barrier function in 3D
473 microvessels. The decline in barrier function commonly observed in primary brain EC *in*
474 *vitro* is often attributed to the loss of tight junctional features [12,27-29], supported by the
475 reduced expression of ZO-1 (*TJP1*) and occludin (*OCLN*) transcript levels found in
476 primary cells in our transcriptomic analysis. Conversely, ETS-iBMEC displayed increased
477 expression of these markers and showed minimum permeability to both low and medium-
478 molecular-weight dextran tracers in a 3D microvascular BBB model, while keeping
479 endothelial ultrastructural morphology, including thin apical-basal height, loss of
480 desmosomes, and lack of microvilli. Future iterations of the model to improve the
481 differentiation toward brain-specific lineage, relevant for cerebral malaria studies, could
482 incorporate FOXF2 and ZIC3, as the recent inducible expression of these brain-specific
483 transcription factors via lentiviral transduction has shown enhanced brain identity and
484 strengthening of barrier properties (*52*). Alternatively, the addition of Wnt activators and
485 TGFβ inhibitors has also recently been shown to further promote brain endothelial
486 specification (*45*).

487 ETS-iBMECs were incorporated in a 3D BBB microvascular model, increasing the
488 physiological complexity through co-culture with astrocytes and pericytes. While this is a

489 proof of concept, in order to implement ETS-iBMECs in more physiologically complex
490 systems, we employed higher throughput 2D microfluidic and real-time impedance-based
491 barrier assays to model *P. falciparum* pathogenesis. These included *in vitro* studies
492 characterising *P. falciparum*-infected RBC sequestration, one of the main hallmarks of
493 severe and cerebral malaria (*53-57*). Perfusion of *P. falciparum*-infected RBC through
494 commercial microfluidic flow chambers revealed strong binding affinity to ETS-iBMECs,
495 supporting their relevance as an alternative model of parasite cytoadherence. The
496 parasite lines used in this study expressed PfEMP1 variants that are highly enriched in
497 severe and cerebral malaria patients (*58-60*). The dual CD36-ICAM 1 binder, ITGICAM1,
498 showed increased binding to ETS-iBMECs compared to iBMEC-*like* and primary brain
499 ECs. ETS-iBMECs expressed the highest levels of ICAM1 under resting conditions and
500 low levels of CD36. Therefore, it is likely that the increased binding of ITGICAM1 is
501 mediated by ICAM1, given its strong affinity to the receptor (*61*). The EPCR binder,
502 IT4var19, also showed increased binding to ETS-iBMECs compared to the other two cell
503 types. Although this phenotype cannot be explained through our transcriptomic analysis,
504 as the expression of *PROCR* (EPCR) was higher in primary brain EC, post-translational
505 modifications or differences in receptor trafficking to the surface may account for the non-
506 significant increase in binding in ETS-iBMECs. The pronounced binding of *P. falciparum*
507 to ETS-iBMECs highlights this model's relevance for studying host–parasite interactions
508 in severe malaria. Future studies could include additional parasite lines with a dual
509 EPCR–ICAM1 binding phenotype (*61, 62*) or samples from patients with severe and
510 uncomplicated malaria to gain deeper insights into disease mechanisms, as cerebral
511 malaria isolates have shown increased affinity for primary brain endothelial cells (*53*).
512 Furthermore, future strategies to gain deeper molecular insights into host–parasite
513 interactions could include knocking out EPCR and ICAM1 in the parental line or
514 introducing point mutations. Therefore, ETS-iBMEC represent an experimentally tractable
515 and physiologically relevant platform to test intervention strategies aimed at reducing *P.*
516 *falciparum* cytoadhesion (*61, 63*),

517 In fatal cases of cerebral malaria, the blood-brain barrier is disrupted, as showing by
518 magnetic resonance imaging scans revealing severe brain swelling (*37, 38*), and by signs
519 of fibrinogen leakage seen in post-mortem samples (*64*). Furthermore, brain vasogenic

520 oedema is not exclusive to severe disease and has also been observed in cases of
521 uncomplicated malaria (*39*). Our previous work, along with others, has shown that *P.*
522 *falciparum* egress in close proximity to endothelial cells is a major driver of barrier
523 breakdown in primary brain EC (*26, 27, 42*). Notably, this phenotype was recapitulated in
524 ETS-iBMECs using impedance-based assays. The disruption was accompanied by a
525 global and homogenous downregulation of almost all transcripts belonging to tight and
526 adherens junctions, among them occludin and ZO-1, previously found decreased in
527 histopathological labelling of cerebral malaria from paediatric (*65*) and adult samples (*66*).
528 Downregulation of vinculin, a focal adhesion junctional protein, was also found in patient
529 post-mortem samples. Although we did not observe a significant downregulation of
530 vinculin upon ETS-iBMEC exposure to parasite products, a significant decrease in
531 expression of almost all other structural and signalling focal adhesion proteins was found.
532 Remarkably, such robust and global downregulation of key regulatory barrier pathways
533 by malaria parasites or products has not been found in previous primary 2D (*42*) or in a
534 3D endothelial-only model (*43*). Alterations in some key genes in these pathways have
535 been identified in our recent *in vitro* primary 3D-BBB model co-cultured with astrocytes
536 and pericytes (*26*), but at a much lower global extent than ETS-iBMECs. This may be a
537 consequence of the greater maturation of endothelial junctions in ETS-iBMECs compared
538 to primary ECs. Alternatively, the global and coordinated response in ETS-iBMECs could
539 result from a more homogenous cellular identity, compared to the heterogeneity observed
540 in primary brain ECs, which arises from their diverse anatomical origin across brain
541 regions and vascular segments (*67*), such as arterioles, capillaries, and venules.

542 Despite these differences in the response to *P. falciparum* between primary brain ECs
543 and ETS-iBMECs, we also identified similarities, such as important transcripts for malaria
544 pathogenesis that were later classified as serum biomarkers of disease (*40, 42*).
545 Furthermore, the ETS-iBMEC model reproduced alterations in angiogenic pathways
546 important for disease, such as VEGF (*68*) and the angiopoietin/tie2 axis. A disruption of
547 the angiopoietin/Tie2 axis has also long been recognised as a biomarker of cerebral
548 malaria (*69-72*), and targeting this pathway has been proposed as a potential therapeutic
549 (*27, 73*). Furthermore, higher concentrations in plasma of VEGF have been found in
550 uncomplicated (*74*) and in the brain of cerebral malaria patients at sites of *P. falciparum*-

551 infected RBC sequestration (*75*) and are strongly associated with patient fatality (*68*).
552 Overall, the ability of ETS-iBMEC to replicate all these relevant pathways of severe
553 disease underscores their ability of iPSC-derived cells to reproduce established relevant
554 molecular signatures of disease.

555 Nonetheless, limitations remain. The differentiation protocols require specialised training
556 and are laborious, and although ETS-iBMECs can be incorporated in complex 3D
557 microvessel models, the low throughput hampers their application to infection research in
558 complex *in vitro* systems. Furthermore, we found that ETS-iBMECs do not activate
559 processes associated with the response to viruses upon challenge with *P. falciparum*-
560 infected RBC products. We have recently shown the importance of the IFN type I and
561 JAK-STAT pathway in *P. falciparum*-mediated barrier disruption in a primary 3D-BBB
562 model. This model showed that ruxolitinib, a JAK-STAT inhibitor, could prevent the loss
563 of vascular integrity, a finding consistent with human clinical trials that revealed the
564 efficacy of ruxolitinib at preventing vascular damage during controlled malaria infections,
565 as well as other parameters associated with severity (*42, 76-78*). Therefore, future
566 improvements in endothelial differentiation approaches should aim to streamline
567 protocols to develop complex 3D assays and enhance innate immune responses in iPSC-
568 derived cells.

569 Nevertheless, the ETS-iBMEC model recapitulates key pathogenic events of severe
570 malaria and opens new avenues for studying its pathogenesis. Future applications of
571 stem-cell technologies could include the generation of models with patient-derived iPSCs,
572 the generation of isogenic multicellular immunocompetent models that could include other
573 perivascular cells, as well as peripheral or tissue resident immune cells from a single
574 donor, given the recently identified importance of T-cells in cerebral malaria (*79, 80*).
575 Other future benefits could include the generation of CRISPR-Cas screenings that could
576 shed light on the molecular mechanisms that drive severe malaria disease pathogenesis
577 (*81*). Overall, ETS-iBMEC-based models establish the value of stem cell-derived systems
578 for *in vitro* studies of severe malaria, paving the way for future advances in disease
579 modelling, therapeutic testing, and mechanistic understanding.

580

581 **Methods**

582 **iPSC culture and differentiation**

583 Human iPSCs (IMR90-4, WiCell Research Institute, Inc.) were maintained on Matrigel-
584 coated dishes with mTeSR1 (Stemcell Technologies) maintenance medium. The DOX-
585 inducible transgenic cell lines for the upregulation of human ETV2, ERG, and FLI1 were
586 generated as follows. Each gene sequence was cloned into the pDONR P5-P2 entry
587 vector, while a modified Tet-One system (Takara Bio) was cloned into the pDONR P1-
588 P5r vector. These entry vectors were then recombined into a piggyBac destination vector
589 containing an antibiotic resistance cassette using the MultiSite Gateway Pro system
590 (ThermoFisher) (*82*). The resulting constructs were electroporated into IMR90-4 iPSCs
591 using the Amaxa 4D-Nucleofector protocol (Lonza), followed by antibiotic selection of the
592 transgenic cells. To assess silencing effects on Tet-One upregulation during
593 differentiation, the same design has been generated with fluorescent reporter proteins.
594 Differentiation has been performed as described (*7*). In brief, iPSCs were seeded as
595 single cells on Matrigel-coated 6-well plates in mTeSR1 with Y-27632 and maintained for
596 two further days in mTeSR1 only. Equally distributed colonies were exposed to
597 unconditioned medium (UM) for six days, containing: 39.25 mL DMEM/F12 (Invitrogen)
598 with 10 mL Knockout Serum Replacement (Gibco), 0.25 mL Glutamax (Invitrogen), 0.5
599 mL non-essential amino acids (Invitrogen) and 0.35 µL ß-mercaptoethanol (Sigma) at 5%
600 O_2. Afterwards, endothelial expansion and transcription factor upregulation were
601 performed for two days in human endothelial serum-free medium (hESFM, Invitrogen),
602 with 1% plasma-derived serum (Sigma), 20 ng/mL hFGF (R&D Systems), and 10 µM
603 retinoic acid (Sigma) for iBMEC-*like* cells. ETS-iBMEC differentiation was promoted
604 through the addition of 100 ng/mL doxycycline. The generated cells were accutase-
605 released, passaged for one hour on collagen-fibronectin-coated wells, washed and used
606 for further assays. TNFα stimulation occurred at 10ng/mL for 18 hours. Mycoplasma tests
607 were performed biweekly.

608

609

610 **Primary cell culture**

611 Primary human brain microvascular endothelial cells (HBMEC, ACBRI 376, Lonza) were
612 cultured in microvascular endothelial cell growth media supplemented with 5% FBS and
613 endothelial supplements (EGM2-MV, Lonza). Primary human astrocytes (HA, ScienCell)
614 were cultured in basal medium supplemented with 2% FBS, 1% Pen-Strep and 1%
615 astrocyte growth factor. Primary human brain vascular pericytes (HBVP, ScienCell) were
616 cultured in basal medium with 2% FBS, 1% Pen-Strep and 1% pericyte growth factor. For
617 culture, all primary cell types were grown in monolayers on Poly-L-lysine-coated flasks
618 with media changes every two days up to 90% confluency. Cells were passaged with
619 Trypsin/EDTA up to passage number 8. Mycoplasma tests were performed biweekly.

620 ***P. falciparum* culture**

621 *P. falciparum* parasite lines HB3var03, IT4var19 (EPCR binding) (*83*) and ITGICAM1
622 (ICAM1 binding) (*84*) were cultured in human O+ erythrocytes in complete media (Gibco
623 RPMI 1640 medium, 10% human type AB-positive plasma, 0.4 mM hypoxanthine, 5 mM
624 glucose, 26.8mM sodium bicarbonate, 1.5 g/L gentamicin), in culture flasks gassed with
625 90% N_2, 5% CO_2 and 1% O_2. Parasites were synchronised twice a week with 5% sorbitol
626 (Sigma) for the synchronisation to ring stages, and 40 mg/mL gelaspan (Braun) for the
627 purification of trophozoites.

628 **3D-BBB fabrication**

629 The generation of 3D microvessels was performed as previously described for blood-
630 brain barrier models (*26, 85*) with either of the three different endothelial cell sources:
631 primary HBMEC, iBMEC-*like* cells and ETS-iBMEC, in combination with primary HA and
632 HBVP. Briefly, type I collagen was isolated from rat tails and dissolved in 0.1% acetic acid
633 (Sigma) at 15mg/mL and then diluted to 7.5 mg/mL in endothelial media supplemented
634 with 1% astrocyte and pericyte growth factor (AGF and PGF). Primary 7.5×10^5 HA/mL
635 and 3.2×10^5 HBVP/mL were added to the neutralised solution before fabrication. The
636 microvascular model was manufactured in a process combining soft lithography and
637 injection moulding as previously described (*85*). The collagen solution containing HA and
638 HBVP was injected on the top and bottom polymeric PMMA jigs previously treated with

639 O_2 plasma. The top part was obtained by negative impression of a polydimethylsiloxane
640 (PDMS) 2-channel pre-patterned microfluidic network. The bottom part was generated
641 through patterning with a flat stamp. Both parts were left for gelation for 1 hour at 37ºC,
642 followed by removal of the PDMS stamps, and top and bottom jigs assembly. For
643 microvessel formation, $7x10^6$ HBMEC/mL were resuspended in EGM2-MV (Lonza) with
644 1% AGF and PGF and seeded in the device by gravity-driven flow. iBMEC-*like* and ETS-
645 iBMEC were seeded at $23x10^6$ cells/mL in hESFM with 1% PDS, AGF and PGF after
646 previous coating with collagen/fibronectin (400/100 ng/mL) for 45 minutes at 37ºC. The
647 microvessels were fed with the respective media twice a day. ETS-iBMEC had continuous
648 DOX exposure until further experimental use.

649 **Immunofluorescence assays**

650 Monolayers and 3D microvessels were fixed in 4% paraformaldehyde for 20 minutes and
651 washed with PBS. The cells were exposed to Background Buster (innovex Bioscience)
652 for 30 minutes and blocked/permeabilised with 2% BSA and 0.1% Triton X-100 in PBS.
653 Primary antibodies for CD31 (BD Pharming, 560983, 1:100), EPCAM (Biolegend,
654 324202, 1:100), ZO-1 (Invitrogen, 40-2200, 1:100), β-catenin (Sanat Cruz Biotech,
655 59737, 1:100), PAR-1 (R&D System, FAB3855G, 1:100), ICAM1 (Abcam, ab20, 1:100)
656 and Phalloidin (Invitrogen A22287, 1:200) were added in blocking solution overnight.
657 Secondary antibodies and DAPI (ThermoFisher, 8 µg/mL) were added after washing for
658 1 hour. After additional washes in PBS, monolayers and microvessels were kept and
659 imaged in PBS. Imaging was performed on an LSM980 Airyscan 2 (Zeiss) and processed
660 using the ZEN imaging software (Zeiss) and Fiji (ImageJ).

661 **Dextran permeability assays**

662 The barrier function of 3D microvessels was tested by permeability assays with low
663 molecular tracers after 4 days in culture in a 37°C microscope environmental chamber on
664 an LSM980 Airyscan 2. Perfusion of 40 kDa (10µM, FITC labelled) and 10 kDa (2 µM,
665 AF647 labelled) fluorescent dextran was performed at a flow rate of 6.5 µL/min, reflecting
666 a wall shear stess of 1 dyn/cm^2 with a withdrawing syringe pimp (Harvard Apparatus, PHD
667 2000). The z-focus was adjusted to the central plane of the vessel, and acquisition

668 intervals of 30 seconds were captured. For quantification, timepoint t_0 was set after full
669 filling of the microvessels with the fluorescent tracer and t_1 after 2.5 minutes of perfusion.
670 Equally sized ROIs (150 µm x 150 µm) were set along the microvessel wall with an equal
671 distribution on the vessel (150 µm x 30 µm) and hydrogel area (150 µm x 120 µm).
672 Apparent microvascular permeability in cm/s was calculated by integrating fluorescence
673 intensity measurements of the set regions between the two timepoints into the following
674 equation: $P = (1 / \Delta t) (V_{gel} / A_v) ((I_{gel1} - I_{gel0}) / (I_{v0} - I_{gel0}))$, in which Δt is the time interval
675 between t_0 and t_1, V_{gel} is the volume of the collagen matrix, A_v the lateral vessel surface,
676 $I_{gel1} - I_{gel0}$ is the difference in measured intensities in the gel area between t_1 and t_0, and
677 I_{v0} is the fluorescent intensity in the vessel at t_0.

678 **Barrier integrity assays by xCELLigence**

679 The ETS-iBMECs were grown on collagen-fibronectin-coated 96-well PET E-plates
680 (Agilent) during real-time cell-index measurements in the xCELLigence RTCA SP reader.
681 Cell attachment and barrier formation was assessed for three days until the cell-index
682 plateaued with a media change every two days. To test for dose-dependent effects on
683 barrier integrity of the egress media, concentrations equivalent to 5, 2.5 and 1.25×10^7
684 ruptured infected RBCs were adjusted with the stock egress media in hESFM with 1%
685 PDS and DOX. After application, the cell index was measured in 15-second intervals in
686 parallel to a media control. All conditions were applied in triplicate, and each experiment
687 was performed with independent ETS-iBMEC differentiations and individual parasite
688 egress media purifications. For analysis, the cell index progression was set to 0 after
689 sample application and sedimentation. The averaged triplicates of the cell index were
690 normalised to the cell index of the media-only control. Area under the curve analysis was
691 performed using GraphPad Prism (version 10.0.2) for experimental times of 12 hours.

692 **Transmission electron microscopy**

693 The 3D microvessels were fixed with 2% PFA and 2.5% GA in endothelial media by
694 perfusion for 30 minutes, followed by two media washes. The device was disassembled,
695 the hydrogel removed from the PMMA jig and cut into small areas. These areas were
696 processed with a secondary fixative (2% PFA, 2.5% GA, 0.25 mM $CaCl_2$, 0.5mM $MgCl_2$,

697 5% sucrose in 0.1% sodium cacodylate in water) over night at 4°C and post-fixed in a
698 reduced osmium solution (1% OsO_4, 1,5% K3F3(III)(CN)6 in 0.065M sodium cacodylate
699 buffer) six times. Post fixation, the hydrogels were incubated for two hours in OsO_4 at 4°C
700 and washed with water six times. The samples were dehydrated in steps of 30, 50, 80,
701 and thrice with 100% ethanol in a PELCO Biowave Pro microwave processor (Ted Pella,
702 Inc.) containing a SteadyTemp Pro and a ColdSpot set to 4°C, with 40 seconds at 250 W
703 each. Infiltration was performed in serial steps of 25, 50, 75, 90, and twice with 100%
704 EPON 812 hard epoxy resin in acetone, assisted by the microwave (3 minutes each at
705 150 W under vacuum) and a final infiltration step in 100% EPON 812 hard epoxy resin
706 overnight at room temperature. In the embedding mould, samples were positioned with
707 the microvessel luminal axis at a 90° angle to the cutting surface to cut transversal
708 sections of the vessel, and then polymerised at 60°C for 48 hours. Microvessel pieces for
709 imaging were randomly selected, and thin sections (70 nm) were retrieved on an
710 ultramicrotome (UC7, Leica Microsystems), collected on formvar-coated slot grids and
711 post-stained in uranyl acetate and lead citrate. Tile montages (12,000x) were acquired on
712 a JEOL JEM 2100 plus at 80 or 120 keV using SerialEM. Montages were processed using
713 IMOD's Blend Montages function and Fiji (ImageJ).

714 ***P. falciparum var* typing and perfusion**

715 For parasite binding assays, *P. falciparum* lines It4var19 and ITGICAM-1 were previously
716 panned and monitored for the respective PfEMP1 variant expression. Briefly, parasites
717 are synchronized with 5% sorbitol and the RNA of ring stage parasites (0-22 h) post-
718 invasion is extracted with Tryzol LS and an RNAeasy kit, and reverse transcribed with
719 TaqManTM Reverse Transcription Reagents (Applied Biosystems, N8080234). The
720 expression of the *var* repertoire is monitored with an IT4 primer repertoire (*86*) with
721 LightCycler 480 SYBR Green I Master (Roche, 04707516001) in a LightCycler 480 II
722 (Roche) following published amplification conditions. Relative transcription of *var* genes
723 was normalized to the housekeeping control seryl-tRNA-synthetase (STS; PF07_0073)
724 and the expression was represented as relative gene expression = 2(- ∆CT). For *P.*
725 *falciparum* binding assays, the synchronised parasite strains were grown to high
726 parasitemia (5-10%) and purified using Percoll (Cytiva) or LD columns (Miltenyi Biotec)

727 to obtain cultures >60% parasitemia. Infected RBCs were stained with PKH67 fluorescent
728 membrane dye (Sigma) and gravity perfused three times at $1x10^7$ infected RBC/mL
729 through endothelial µ-slides VI 0.1 (ibidi) channels previously seeded three days before
730 with iBMEC-*like*, ETS-iBMEC and primary brain EC. After parasite perfusion, unbound
731 parasites were washed out with media for 10 minutes, and the endothelial channels were
732 fixed with 4% PFA in PBS for 15 minutes and washed with PBS. After fixation, endothelial
733 nuclei were stained with DAPI (8 µg/mL), and the channels were imaged using confocal
734 microscopy on an LSM980 Airyscan 2 (Zeiss) and processed using Fiji (ImageJ). Up to
735 nine ROIs of equal size were selected per channel and bound parasites quantified using
736 Fiji.

737 **Parasite egress media preparation**

738 Parasite egress products were purified by tightly synchronising *P. falciparum*-infected
739 RBC HB3var03 parasites into a 6-hour window. Late-stage parasites, approximately at
740 44 hpi, were enriched to $5x10^7$ infected RBC/mL using Percoll purification, and incubated
741 in complete media with 1 µM compound 2, which inhibits schizont egress (a reversible
742 PKG inhibitor kindly provided by Michael Blackman, The Francis Crick Institute). After 5
743 hours, simultaneous schizont rupture was induced by resuspending parasites in
744 endothelial media without compound 2 at a concentration of 10^8 schizonts/mL overnight
745 at 30 rpm on a shaker. The total rupture efficiency was assessed by a hemocytometer
746 count, and Giemsa blood smear and supernatants were recovered after spinning at 1000
747 rpm and snap frozen in liquid nitrogen. For experimental use, the concentration of rupture
748 released factors was adjusted to the equivalent of 5, 2.5 and $1.25x10^7$ ruptured
749 schizonts/mL, which represents the physiological simultaneous release during approx.
750 1% parasitemia within one asexual blood cycle (*37*).

751 **Bulk RNA-sequencing and analysis**

752 For transcriptional analysis, bulk RNA sequencing data were generated from primary
753 brain EC, iBMEC-*like* cells, and ETS-iBMEC. Cells were cultured as 2D monolayers for
754 three days on 24-well plates and exposed to egress products from ruptured schizonts
755 ($5x10^7$ schizonts/mL) or a media control. The experimental design included exposure

durations of 8 and 24 hours to examine transcriptional responses over time. Samples were fixed with RLT buffer, and RNA was extracted using the RNeasy Mini kit (QIAgen), including DNAse treatment. Quality and RNA concentration were assessed by TapeStation (Agilent). Individually barcoded stranded mRNA-seq libraries were prepared from high-quality total RNA samples (~100 ng/sample) using the New England Biolabs NEBNext RNA Ultra II Kit combined with the polyA-enrichment module in 12 PCR cycles on a liquid handling robot (Beckman i7). The resulting libraries were pooled in equimolar amounts and loaded on the Illumina sequencer NextSeq 2000 platform, sequencing unidirectionally, generating 1980 million reads, each 80 bases long.

Raw reads were assessed for quality using FastQC (version 0.12.1). Transcript quantification was performed using Salmon (v1.10.3) with an index built from the Ensembl GRCh38 reference transcriptome (*87*). Transcript-level abundances from Salmon were imported into R and summarised to gene level using the tximport package (v1.32.0) (*88*), with transcript-to-gene mappings derived from the corresponding Ensembl GTF annotation. Only protein-coding genes were retained for further analysis, as determined by annotation with org.Hs.eg.db (v3.19.1). Genes with low read counts were filtered out (<10 counts in at least one sample) before differential expression analysis, which was performed using DESeq2 (v1.44.0) (*89*). Log fold change shrinkage was applied with apeglm (v1.26.1) for more stable effect size estimation (*90*). P-values were adjusted for multiple testing using the Benjamini-Hochberg procedure. Genes with adjusted p-value < 0.05 and $|\log_2$ fold change$|$ > 0.1 were considered significantly differentially expressed. Log_2 fold changes (LFCs) for selected gene sets of interest were extracted from DESeq2 differential expression results. Heatmaps were generated using the pheatmap package (v1.0.12) (*91*). GO over-representation analysis of differentially expressed genes was performed using the clusterProfiler package (v4.12.6) (*92*). Ensembl gene identifiers were mapped to Entrez IDs using org.Hs.eg.db. GO over-representation was carried out for biological process terms. GO term maps (emapplots) were generated with enrichplot (v1.24.4) to display similarity networks of enriched processes, showing clusters of functionally related terms among up- or downregulated gene sets with a semantic similarity score ≥ 0.15 (*93*). Volcano plots were visualised using the EnhancedVolcano package (v1.22.0) (*94*). Endothelial and epithelial gene sets were highlighted using

787 curated gene lists from endothelial (red) or epithelial (blue) GO terms. Marker genes from
788 each group with a described endothelial or epithelial function were labelled. Variance
789 stabilising transformation was performed to generate normalised gene expression
790 heatmap visualisations. A curated set of genes of interest was selected, and their
791 expression values were averaged for each condition. The centered, normalised
792 expression values were visualized as heatmaps using the pheatmap package, with
793 clustering performed on columns (conditions).

794 **Detection of alternative splicing events and analysis**

795 Alternative splicing profiles have been generated using vast-tools, which aligns and
796 processes raw RNA-seq reads to derive PSI (percent spliced in) values for all types of
797 AS events. *Homo sapiens* (hg38, Hs2), with Ensembl v88 scaffold annotation was used
798 for event detection. Differentially spliced events between the media and the 24 hour
799 timepoint condition were considered when ΔPSI was at least 15. The potential impact of
800 splicing on the proteome was based on data from VastDB (*36*).

801 **Statistical analysis**

802 All statistical tests were performed with GraphPad Prism. Shapiro-Wilk test has been
803 used to test normality. One-way ANOVA was used for testing differences between groups
804 in normally distributed data. For nonparametric data, Mann-Whitney U test has been
805 performed to test differences between two groups, and Dunn's multiple comparison test
806 was used to compare multiple pairs within the dataset.

807 **Data availability**

808 RNA-seq datasets generated and used in this study are available in the ArrayExpress
809 database under the accession code E-MTAB-14937.

810 **Author contributions**

811 FK and MB conceived the work. FK, HF, RL, LP, ME and MB designed the experiments.
812 FK, HF, LP, BG, and DC performed the experiments. FK analysed the experimental data
813 under the guidance of ME and MB. PP analysed splicing events under the supervision of

VT. AB gave guidance on RNA-seq analysis performed by FK. FK and MB wrote the original draft of the manuscript. All authors contributed to the manuscript revision, editing and suggestions. FK, ME and MB contributed to project supervision, administration and funding acquisition.

Acknowledgments

We want to thank all members of the Bernabeu and Ebisuya labs for their supportive discussion and critical feedback. We want to thank Mitsuhiro Matsuda for the support and mentoring with the stem cell technologies. Furthermore, we want to thank Jorge Trojanowski for input on the RNA-seq experimental preparation and analysis, Jaroslaw Sochacki, Jorge Lázaro, and Laura Batlle for feedback on iPSC culture, Michael Blackman (The Francis Crick Institute) for kindly providing compound 2 and Knut Woltjen for providing the piggyBac vector.

We thank Vladimir Benes and the Genomics Core facility (Gene Core) at EMBL, the Genomics Core facility at the Universitat Pompeu Fabra (UPF), Charles Girardot and the Genome Biological Support (GBCS) at EMBL for their support in RNA sequencing and the Electron Microscopy Core Facility (EMCF) at EMBL for their support with EM imaging. This work was supported by the European Research Council (ERC), the European Union's Horizon 2020 research and innovation program (Grant agreement No. 948088 to MB and No. 101002564 to ME), the Deutsche Forschungsgemeinschaft (DFG, German Research Foundation) under Germany's Excellence Strategy - EXC 2068 - 390729961 - Cluster of Excellence Physics of Life of TU Dresden, the Alexander von Humboldt Foundation, and the Marie Skłodowska-Curie Actions COFUND (847543) with additional funds from the EMBL core program and the EMBL Infection Biology Transversal Theme.

837 ## Literature

838 1. W. H. Organization, *World malaria report 2023*. (World Health Organization, 2023).
839 2. M. F. Sabbagh, J. Nathans, A genome-wide view of the de-differentiation of central nervous
840 system endothelial cells in culture. *Elife* **9**, e51276 (2020).
841 3. E. S. Egan *et al.*, Malaria. A forward genetic screen identifies erythrocyte CD55 as essential for
842 Plasmodium falciparum invasion. *Science* **348**, 711-714 (2015).
843 4. E. S. Egan, Beyond Hemoglobin: Screening for Malaria Host Factors. *Trends Genet* **34**, 133-141
844 (2018).
845 5. A. Pance *et al.*, Novel stem cell technologies are powerful tools to understand the impact of
846 human factors on Plasmodium falciparum malaria. *Front Cell Infect Microbiol* **13**, 1287355
847 (2023).
848 6. E. S. Lippmann *et al.*, Derivation of blood-brain barrier endothelial cells from human pluripotent
849 stem cells. *Nature biotechnology* **30**, 783-791 (2012).
850 7. T.-E. Park *et al.*, Hypoxia-enhanced Blood-Brain Barrier Chip recapitulates human barrier
851 function and shuttling of drugs and antibodies. *Nature communications* **10**, 2621 (2019).
852 8. T. M. Lu *et al.*, Pluripotent stem cell-derived epithelium misidentified as brain microvascular
853 endothelium requires ETS factors to acquire vascular fate. *Proceedings of the National Academy*
854 *of Sciences* **118**, e2016950118 (2021).
855 9. Y. Ding, S. P. Palecek, E. V. Shusta, iPSC-derived blood-brain barrier modeling reveals APOE
856 isoform-dependent interactions with amyloid beta. *Fluids and Barriers of the CNS* **21**, 79 (2024).
857 10. P. P. Mondkar, H. S. Seo, T. P. Lodge, S. M. Azarin, Diblock Copolymers of Poly (ethylene oxide)-
858 b-poly (propylene oxide) Stabilize a Blood–Brain Barrier Model under Oxidative Stress.
859 *Molecular pharmaceutics* **21**, 5646-5660 (2024).
860 11. H. Nishihara *et al.*, Intrinsic blood–brain barrier dysfunction contributes to multiple sclerosis
861 pathogenesis. *Brain* **145**, 4334-4348 (2022).
862 12. A. Gopinadhan *et al.*, A human pluripotent stem cell-derived in vitro model of the blood-brain
863 barrier in cerebral malaria. *Fluids Barriers CNS* **21**, 38 (2024).
864 13. K. Wang *et al.*, Robust differentiation of human pluripotent stem cells into endothelial cells via
865 temporal modulation of ETV2 with modified mRNA. *Sci Adv* **6**, eaba7606 (2020).
866 14. T. M. Lu *et al.*, Human Induced Pluripotent Stem Cell-Derived Brain Endothelial Cells: Current
867 Controversies. *Front Physiol* **12**, 642812 (2021).
868 15. R. Morita *et al.*, ETS transcription factor ETV2 directly converts human fibroblasts into functional
869 endothelial cells. *Proc Natl Acad Sci U S A* **112**, 160-165 (2015).
870 16. A. G. Lindgren, M. B. Veldman, S. Lin, ETV2 expression increases the efficiency of primitive
871 endothelial cell derivation from human embryonic stem cells. *Cell Regen* **4**, 1 (2015).
872 17. H. Zhang, T. Yamaguchi, Y. Kokubu, K. Kawabata, Transient ETV2 Expression Promotes the
873 Generation of Mature Endothelial Cells from Human Pluripotent Stem Cells. *Biol Pharm Bull* **45**,
874 483-490 (2022).
875 18. N. Koyano-Nakagawa, D. J. Garry, Etv2 as an essential regulator of mesodermal lineage
876 development. *Cardiovascular research* **113**, 1294-1306 (2017).
877 19. W. Gong *et al.*, ETV2 functions as a pioneer factor to regulate and reprogram the endothelial
878 lineage. *Nature cell biology* **24**, 672-684 (2022).
879 20. N. Nagai *et al.*, Downregulation of ERG and FLI1 expression in endothelial cells triggers
880 endothelial-to-mesenchymal transition. *PLoS genetics* **14**, e1007826 (2018).
881 21. D. D. Spyropoulos *et al.*, Hemorrhage, impaired hematopoiesis, and lethality in mouse embryos
882 carrying a targeted disruption of the Fli1 transcription factor. *Molecular and cellular biology* **20**,
883 5643-5652 (2000).

884 22. M. J. Stebbins *et al.*, Differentiation and characterization of human pluripotent stem cell-derived
885 brain microvascular endothelial cells. *Methods* **101**, 93-102 (2016).
886 23. G. Helms, A. K. Dasanna, U. S. Schwarz, M. Lanzer, Modeling cytoadhesion of Plasmodium
887 falciparum-infected erythrocytes and leukocytes-common principles and distinctive features.
888 *FEBS Lett* **590**, 1955-1971 (2016).
889 24. M. Bernabeu, J. D. Smith, EPCR and Malaria Severity: The Center of a Perfect Storm. *Trends*
890 *Parasitol* **33**, 295-308 (2017).
891 25. Y. Zheng *et al.*, In vitro microvessels for the study of angiogenesis and thrombosis. *Proc Natl*
892 *Acad Sci U S A* **109**, 9342-9347 (2012).
893 26. L. Piatti *et al.*, Pathogenic mechanisms of Plasmodium falciparum egress unveiled by
894 a microvascular 3D blood-brain barrier model. *bioRxiv*, 2024.2010.2015.618439 (2024).
895 27. R. K. Long *et al.*, Plasmodium falciparum disruption of pericyte angiopoietin-1 secretion
896 contributes to barrier breakdown in a 3D brain microvessel model. *bioRxiv*, 2024.2003.
897 2029.587334 (2024).
898 28. T. Lavstsen *et al.*, Plasmodium falciparum erythrocyte membrane protein 1 domain cassettes 8
899 and 13 are associated with severe malaria in children. *Proc Natl Acad Sci U S A* **109**, E1791-1800
900 (2012).
901 29. L. Turner *et al.*, Severe malaria is associated with parasite binding to endothelial protein C
902 receptor. *Nature* **498**, 502-505 (2013).
903 30. M. Bernabeu *et al.*, Severe adult malaria is associated with specific PfEMP1 adhesion types and
904 high parasite biomass. *Proc Natl Acad Sci U S A* **113**, E3270-3279 (2016).
905 31. A. Kessler *et al.*, Linking EPCR-Binding PfEMP1 to Brain Swelling in Pediatric Cerebral Malaria.
906 *Cell Host Microbe* **22**, 601-614 e605 (2017).
907 32. P. K. Sahu *et al.*, Determinants of brain swelling in pediatric and adult cerebral malaria. *JCI*
908 *Insight* **6**, (2021).
909 33. M. R. Gillrie *et al.*, Src-family kinase dependent disruption of endothelial barrier function by
910 Plasmodium falciparum merozoite proteins. *Blood* **110**, 3426-3435 (2007).
911 34. M. R. Gillrie *et al.*, Plasmodium falciparum histones induce endothelial proinflammatory
912 response and barrier dysfunction. *Am J Pathol* **180**, 1028-1039 (2012).
913 35. J. Gallego-Delgado *et al.*, Angiotensin receptors and beta-catenin regulate brain endothelial
914 integrity in malaria. *J Clin Invest* **126**, 4016-4029 (2016).
915 36. J. Tapial *et al.*, An atlas of alternative splicing profiles and functional associations reveals new
916 regulatory programs and genes that simultaneously express multiple major isoforms. *Genome*
917 *Res* **27**, 1759-1768 (2017).
918 37. K. B. Seydel *et al.*, Brain swelling and death in children with cerebral malaria. *N Engl J Med* **372**,
919 1126-1137 (2015).
920 38. P. K. Sahu *et al.*, Brain magnetic resonance imaging reveals different courses of disease in
921 pediatric and adult cerebral malaria. *Clinical Infectious Diseases* **73**, e2387-e2396 (2021).
922 39. S. Mohanty *et al.*, Evidence of Brain Alterations in Noncerebral Falciparum Malaria. *Clin Infect*
923 *Dis* **75**, 11-18 (2022).
924 40. C. Gomes *et al.*, Endothelial transcriptomic analysis identifies biomarkers of severe and cerebral
925 malaria. *JCI Insight* **8**, (2023).
926 41. A. K. Tripathi, W. Sha, V. Shulaev, M. F. Stins, D. J. Sullivan, Jr., Plasmodium falciparum-infected
927 erythrocytes induce NF-kappaB regulated inflammatory pathways in human cerebral
928 endothelium. *Blood* **114**, 4243-4252 (2009).
929 42. M. Zuniga *et al.*, Plasmodium falciparum and TNF-alpha Differentially Regulate Inflammatory
930 and Barrier Integrity Pathways in Human Brain Endothelial Cells. *mBio* **13**, e0174622 (2022).

931 43. C. Howard, F. Joof, R. Hu, J. D. Smith, Y. Zheng, Probing cerebral malaria inflammation in 3D
932 human brain microvessels. *Cell Rep* **42**, 113253 (2023).
933 44. J. M. Gomez-Salinero *et al.*, Cooperative ETS Transcription Factors Enforce Adult Endothelial Cell
934 Fate and Cardiovascular Homeostasis. *Nat Cardiovasc Res* **1**, 882-899 (2022).
935 45. Y. Ding *et al.*, ETV2 Overexpression Promotes Efficient Differentiation of Pluripotent Stem Cells
936 to Endothelial Cells. *Biotechnol Bioeng* **122**, 1914-1928 (2025).
937 46. D. Chen *et al.*, Pioneer factor ETV2 safeguards endothelial cell specification by recruiting the
938 repressor REST to restrict alternative lineage commitment. *Nat Cardiovasc Res* **4**, 689-709
939 (2025).
940 47. L. Gong *et al.*, Rapid generation of functional vascular organoids via simultaneous transcription
941 factor activation of endothelial and mural lineages. *Cell Stem Cell*, (2025).
942 48. A. H. M. Ng *et al.*, A comprehensive library of human transcription factors for cell fate
943 engineering. *Nat Biotechnol* **39**, 510-519 (2021).
944 49. J. M. Gomez-Salinero, D. Redmond, S. Rafii, Microenvironmental determinants of endothelial
945 cell heterogeneity. *Nat Rev Mol Cell Biol* **26**, 476-495 (2025).
946 50. S. Rieck *et al.*, Forward programming of human induced pluripotent stem cells via the ETS
947 variant transcription factor 2: rapid, reproducible, and cost-effective generation of highly
948 enriched, functional endothelial cells. *Cardiovasc Res* **120**, 1472-1484 (2024).
949 51. A. C. Luo *et al.*, A streamlined method to generate endothelial cells from human pluripotent
950 stem cells via transient doxycycline-inducible ETV2 activation. *Angiogenesis* **27**, 779-795 (2024).
951 52. A. Cui *et al.*, Generation of hiPSC-derived brain microvascular endothelial cells using a
952 combination of directed differentiation and transcriptional reprogramming strategies. *bioRxiv*,
953 (2024).
954 53. J. Storm *et al.*, Cerebral malaria is associated with differential cytoadherence to brain
955 endothelial cells. *EMBO Mol Med* **11**, (2019).
956 54. M. J. Ponsford *et al.*, Sequestration and microvascular congestion are associated with coma in
957 human cerebral malaria. *J Infect Dis* **205**, 663-671 (2012).
958 55. J. Hanson *et al.*, Microvascular obstruction and endothelial activation are independently
959 associated with the clinical manifestations of severe falciparum malaria in adults: an
960 observational study. *BMC Med* **13**, 122 (2015).
961 56. A. M. Dondorp *et al.*, Direct in vivo assessment of microcirculatory dysfunction in severe
962 falciparum malaria. *J Infect Dis* **197**, 79-84 (2008).
963 57. J. Hanson *et al.*, Relative contributions of macrovascular and microvascular dysfunction to
964 disease severity in falciparum malaria. *J Infect Dis* **206**, 571-579 (2012).
965 58. M. Avril, M. Bernabeu, M. Benjamin, A. J. Brazier, J. D. Smith, Interaction between Endothelial
966 Protein C Receptor and Intercellular Adhesion Molecule 1 to Mediate Binding of Plasmodium
967 falciparum-Infected Erythrocytes to Endothelial Cells. *mBio* **7**, (2016).
968 59. A. R. Berendt, D. L. Simmons, J. Tansey, C. I. Newbold, K. Marsh, Intercellular adhesion molecule-
969 1 is an endothelial cell adhesion receptor for Plasmodium falciparum. *Nature* **341**, 57-59 (1989).
970 60. J. A. Rowe, A. Claessens, R. A. Corrigan, M. Arman, Adhesion of Plasmodium falciparum-infected
971 erythrocytes to human cells: molecular mechanisms and therapeutic implications. *Expert Rev*
972 *Mol Med* **11**, e16 (2009).
973 61. M. Bernabeu *et al.*, Binding Heterogeneity of Plasmodium falciparum to Engineered 3D Brain
974 Microvessels Is Mediated by EPCR and ICAM-1. *mBio* **10**, (2019).
975 62. R. A. Reyes *et al.*, Broadly inhibitory antibodies to severe malaria virulence proteins. *Nature* **636**,
976 182-189 (2024).
977 63. F. Joof *et al.*, Plasma From Older Children in Malawi Inhibits Plasmodium falciparum Binding in
978 3-Dimensional Brain Microvessels. *J Infect Dis* **230**, e1402-e1411 (2024).

979 64. K. Dorovini-Zis *et al.*, The Neuropathology of Fatal Cerebral Malaria in Malawian Children. *The*
980 *American Journal of Pathology* **178**, 2146-2158 (2011).
981 65. H. Brown *et al.*, Blood-brain barrier function in cerebral malaria in Malawian children. *Am J Trop*
982 *Med Hyg* **64**, 207-213 (2001).
983 66. H. Brown *et al.*, Evidence of blood-brain barrier dysfunction in human cerebral malaria.
984 *Neuropathol Appl Neurobiol* **25**, 331-340 (1999).
985 67. T. Walchli *et al.*, Single-cell atlas of the human brain vasculature across development, adulthood
986 and disease. *Nature* **632**, 603-613 (2024).
987 68. V. Jain *et al.*, Plasma IP-10, apoptotic and angiogenic factors associated with fatal cerebral
988 malaria in India. *Malar J* **7**, 83 (2008).
989 69. A. L. Conroy *et al.*, Whole blood angiopoietin-1 and -2 levels discriminate cerebral and severe
990 (non-cerebral) malaria from uncomplicated malaria. *Malar J* **8**, 295 (2009).
991 70. A. L. Conroy *et al.*, Angiopoietin-2 levels are associated with retinopathy and predict mortality in
992 Malawian children with cerebral malaria: a retrospective case-control study*. *Crit Care Med* **40**,
993 952-959 (2012).
994 71. F. E. Lovegrove *et al.*, Serum angiopoietin-1 and -2 levels discriminate cerebral malaria from
995 uncomplicated malaria and predict clinical outcome in African children. *PLoS One* **4**, e4912
996 (2009).
997 72. T. W. Yeo *et al.*, Angiopoietin-2 is associated with decreased endothelial nitric oxide and poor
998 clinical outcome in severe falciparum malaria. *Proc Natl Acad Sci U S A* **105**, 17097-17102 (2008).
999 73. S. J. Higgins *et al.*, Dysregulation of angiopoietin-1 plays a mechanistic role in the pathogenesis
1000 of cerebral malaria. *Sci Transl Med* **8**, 358ra128 (2016).
1001 74. T. Furuta, M. Kimura, N. Watanabe, Elevated levels of vascular endothelial growth factor (VEGF)
1002 and soluble vascular endothelial growth factor receptor (VEGFR)-2 in human malaria. *Am J Trop*
1003 *Med Hyg* **82**, 136-139 (2010).
1004 75. I. M. Medana *et al.*, Induction of the vascular endothelial growth factor pathway in the brain of
1005 adults with fatal falciparum malaria is a non-specific response to severe disease. *Histopathology*
1006 **57**, 282-294 (2010).
1007 76. R. Webster *et al.*, Adjunctive ruxolitinib attenuates inflammation and enhances antiparasitic
1008 immunity in human volunteers experimentally infected with Plasmodium falciparum. *MedRxiv*,
1009 2025.2003. 2026.25324737 (2025).
1010 77. L. Bukali *et al.*, Transient JAK/STAT inhibition by ruxolitinib modulates malaria-specific CD4+ T
1011 cell responses and enhances recall immunity in volunteers experimentally infected with
1012 Plasmodium falciparum. *medRxiv*, 2025.2004. 2009.25325416 (2025).
1013 78. M. F. Chughlay *et al.*, Safety, Tolerability, Pharmacokinetics, and Pharmacodynamics of
1014 Coadministered Ruxolitinib and Artemether-Lumefantrine in Healthy Adults. *Antimicrobial*
1015 *Agents and Chemotherapy* **66**, e01584-01521 (2022).
1016 79. V. Barrera *et al.*, Comparison of CD8(+) T Cell Accumulation in the Brain During Human and
1017 Murine Cerebral Malaria. *Front Immunol* **10**, 1747 (2019).
1018 80. B. A. Riggle *et al.*, CD8+ T cells target cerebrovasculature in children with cerebral malaria. *J Clin*
1019 *Invest* **130**, 1128-1138 (2020).
1020 81. F. Korbmacher, M. Bernabeu, Induced pluripotent stem cell-based tissue models to study
1021 malaria: a new player in the research game. *Curr Opin Microbiol* **84**, 102585 (2025).
1022 82. K. Woltjen *et al.*, piggyBac transposition reprograms fibroblasts to induced pluripotent stem
1023 cells. *Nature* **458**, 766-770 (2009).
1024 83. M. Avril *et al.*, A restricted subset of var genes mediates adherence of Plasmodium falciparum-
1025 infected erythrocytes to brain endothelial cells. *Proc Natl Acad Sci U S A* **109**, E1782-1790 (2012).

1026 84. C. F. Ockenhouse *et al.*, Human vascular endothelial cell adhesion receptors for Plasmodium
1027 falciparum-infected erythrocytes: roles for endothelial leukocyte adhesion molecule 1 and
1028 vascular cell adhesion molecule 1. *J Exp Med* **176**, 1183-1189 (1992).
1029 85. L. Piatti, C. C. Howard, Y. Zheng, M. Bernabeu, Binding of Plasmodium falciparum-Infected Red
1030 Blood Cells to Engineered 3D Microvessels. *Methods Mol Biol* **2470**, 557-585 (2022).
1031 86. J. H. Janes *et al.*, Investigating the host binding signature on the Plasmodium falciparum PfEMP1
1032 protein family. *PLoS Pathog* **7**, e1002032 (2011).
1033 87. R. Patro, G. Duggal, M. I. Love, R. A. Irizarry, C. Kingsford, Salmon provides fast and bias-aware
1034 quantification of transcript expression. *Nat Methods* **14**, 417-419 (2017).
1035 88. C. Soneson, M. I. Love, M. D. Robinson, Differential analyses for RNA-seq: transcript-level
1036 estimates improve gene-level inferences. *F1000Res* **4**, 1521 (2015).
1037 89. M. I. Love, W. Huber, S. Anders, Moderated estimation of fold change and dispersion for RNA-
1038 seq data with DESeq2. *Genome Biol* **15**, 550 (2014).
1039 90. A. Zhu, J. G. Ibrahim, M. I. Love, Heavy-tailed prior distributions for sequence count data:
1040 removing the noise and preserving large differences. *Bioinformatics* **35**, 2084-2092 (2019).
1041 91. R. Kolde. (2019).
1042 92. T. Wu *et al.*, clusterProfiler 4.0: A universal enrichment tool for interpreting omics data. *The*
1043 *innovation* **2**, (2021).
1044 93. G. Yu. (2024).
1045 94. K. Blighe, S. Rana, M. Lewis. (2024).

1046

1047

1048

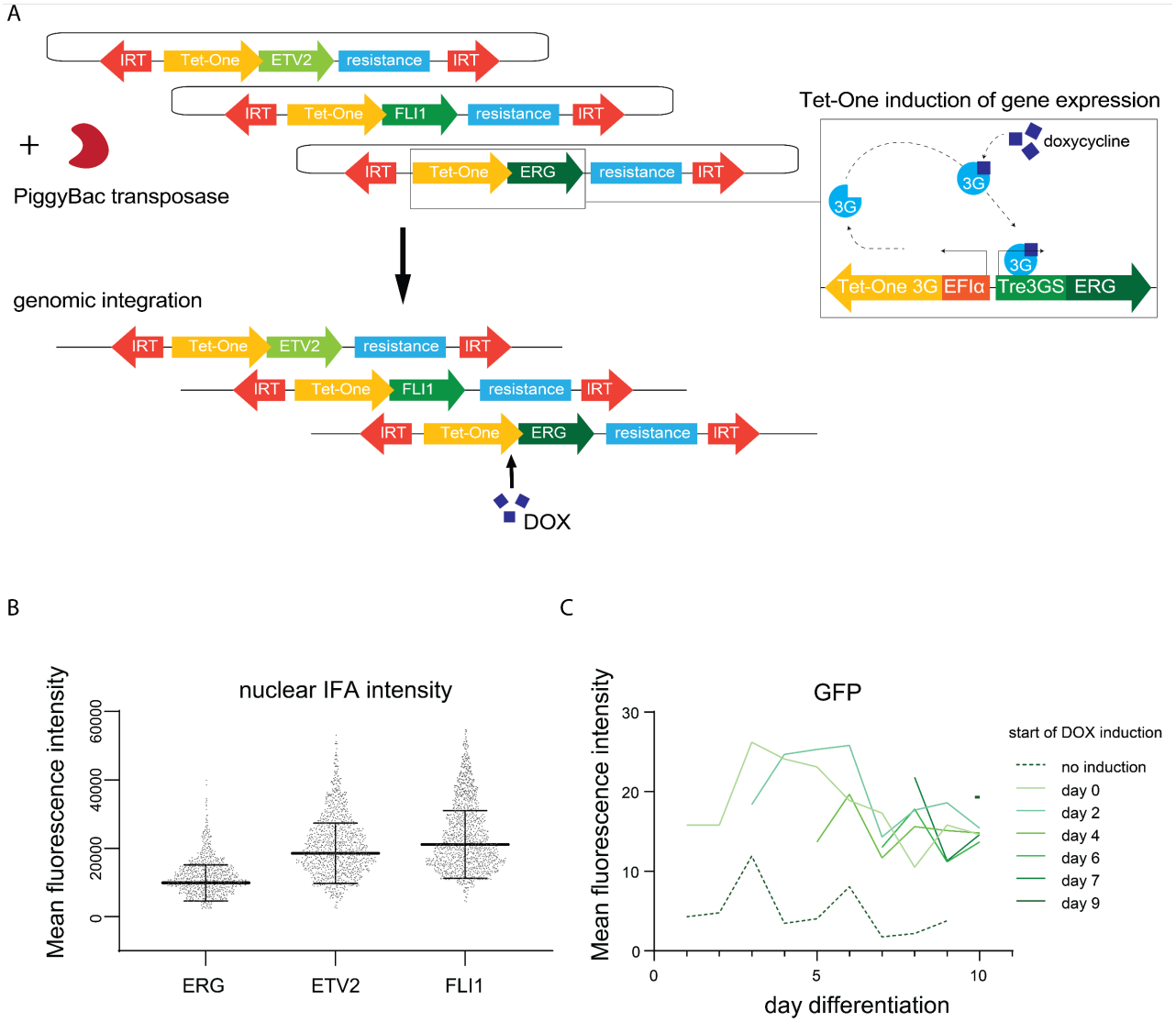

Fig. S1 - ETS-transcription factor upregulation in ETS-iBMEC. (**A**) Simplified schematic representation of the strategy used to generate transgenic iPSCs harbouring a DOX-inducible Tet-One system for the upregulation of the ETS-transcription factors ETV2, FLI1, and ERG. Constructs are integrated into the genome using PiggyBac transposase. (**B**) Expression analysis of nuclear immunofluorescence intensity for ERG, ETV2 and FLI1 in a selected clonal line following DOX-induction. Each dot represents the nucleus of a single cell. Bars indicate mean and standard deviation. (**C**) Stepwise DOX induction of transgenic iPSCs carrying a Tet-One inducible fluorescent reporter (exemplified by GFP) and differentiated towards iBMEC-*like* cells. Fluorescence intensity was measured daily by fluorescence microscopy.

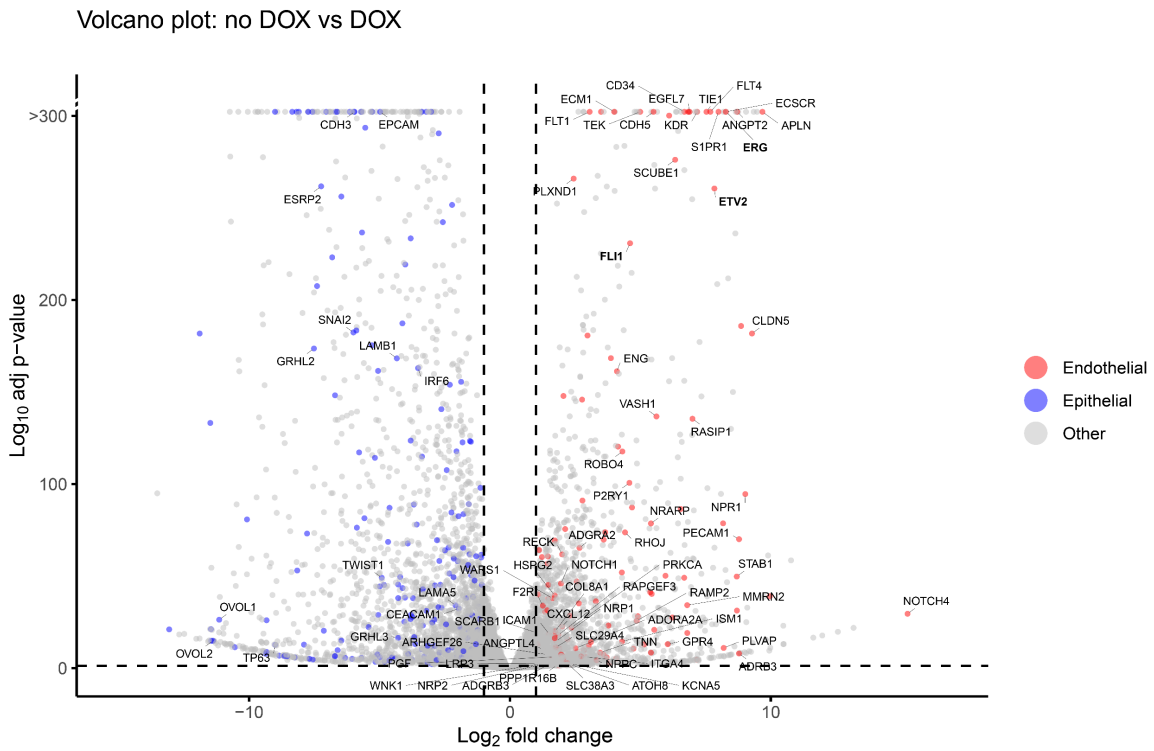

Fig. S2 - Differential gene expression between non-induced iBMEC-*like* cells and DOX-induced ETS-iBMECs. Enhanced Volcano plot showing differentially expressed genes (adjusted p-value < 0.05, Log_2 fold change > ±1) between both cell types at day 11 of differentiation. Genes associated with endothelial (red) or epithelial (blue) GO terms are color-coded. Selected endothelial and epithelial genes are labelled with their gene symbols.

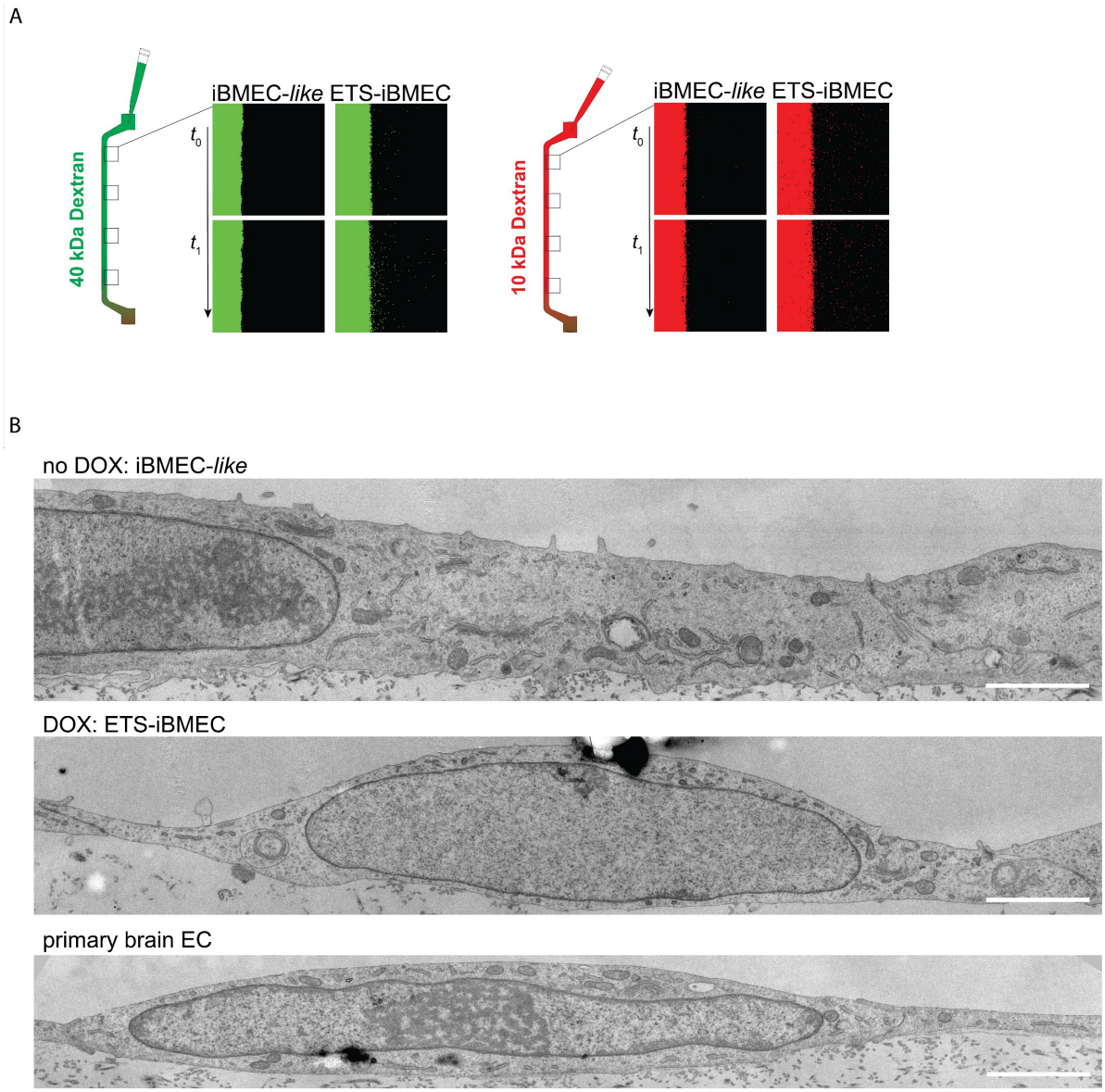

Fig. S3 – Functional and ultrastructural assays in 3D *in vitro* BBB microvessels. (**A**) Permeability of iBMEC-*like* and ETS-iBMEC microvessels perfused with fluorescently labelled 40 kDa FITC dextran (green) 10 kDa AF647 dextran (red). Apparent permeability is analysed in squared regions at two different timepoints of perfusion (t_1 = 150 seconds). (**B**) TEM imaging of iBMEC-*like*, ETS-iBMEC and primary brain EC (scale bars: 2 µm).

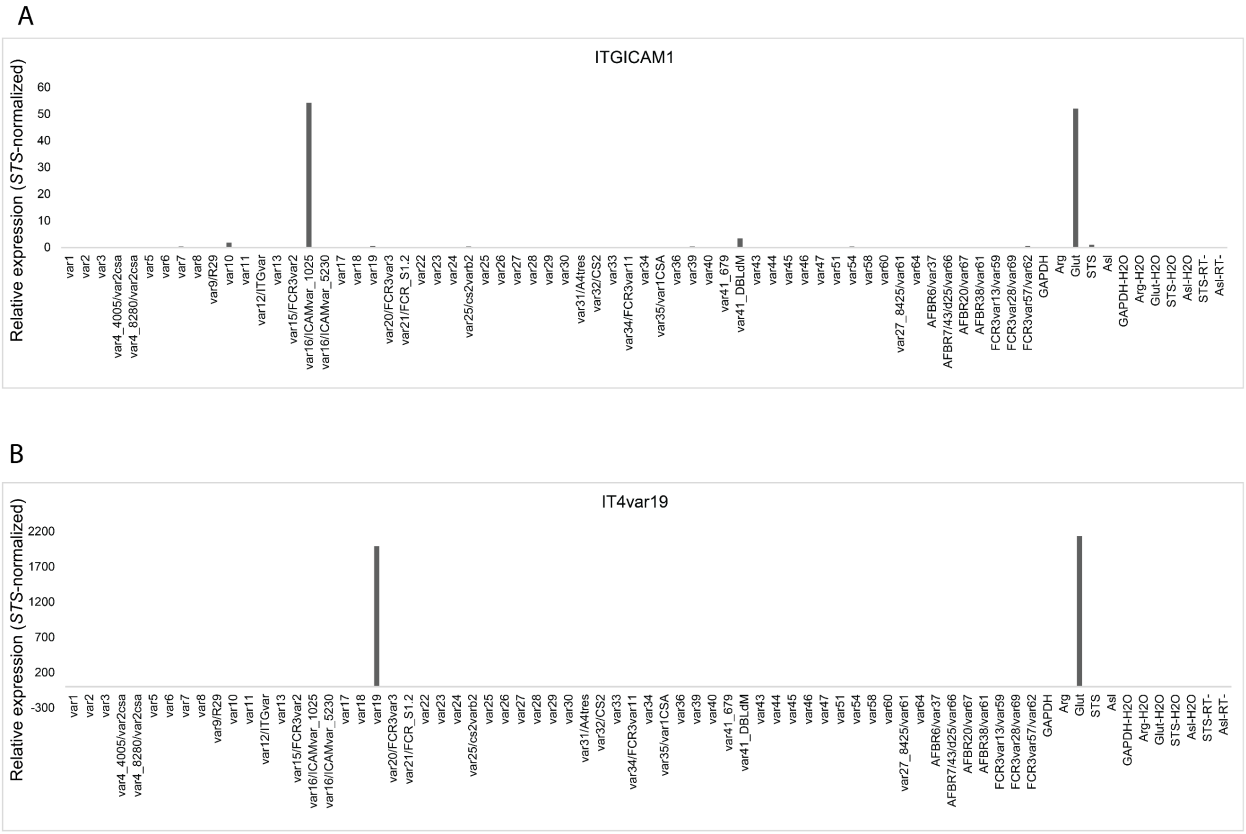

Fig. S4 – PfEMP1 variant predominant expression analysis by real-time PCR. Confirmation of (**A**) ITGICAM1 and (**B**) IT4var19 expression with *var* strain-specific primers, together with housekeeping genes to confirm the correct *var* gene expression. Relative gene expression normalized to *STS.*

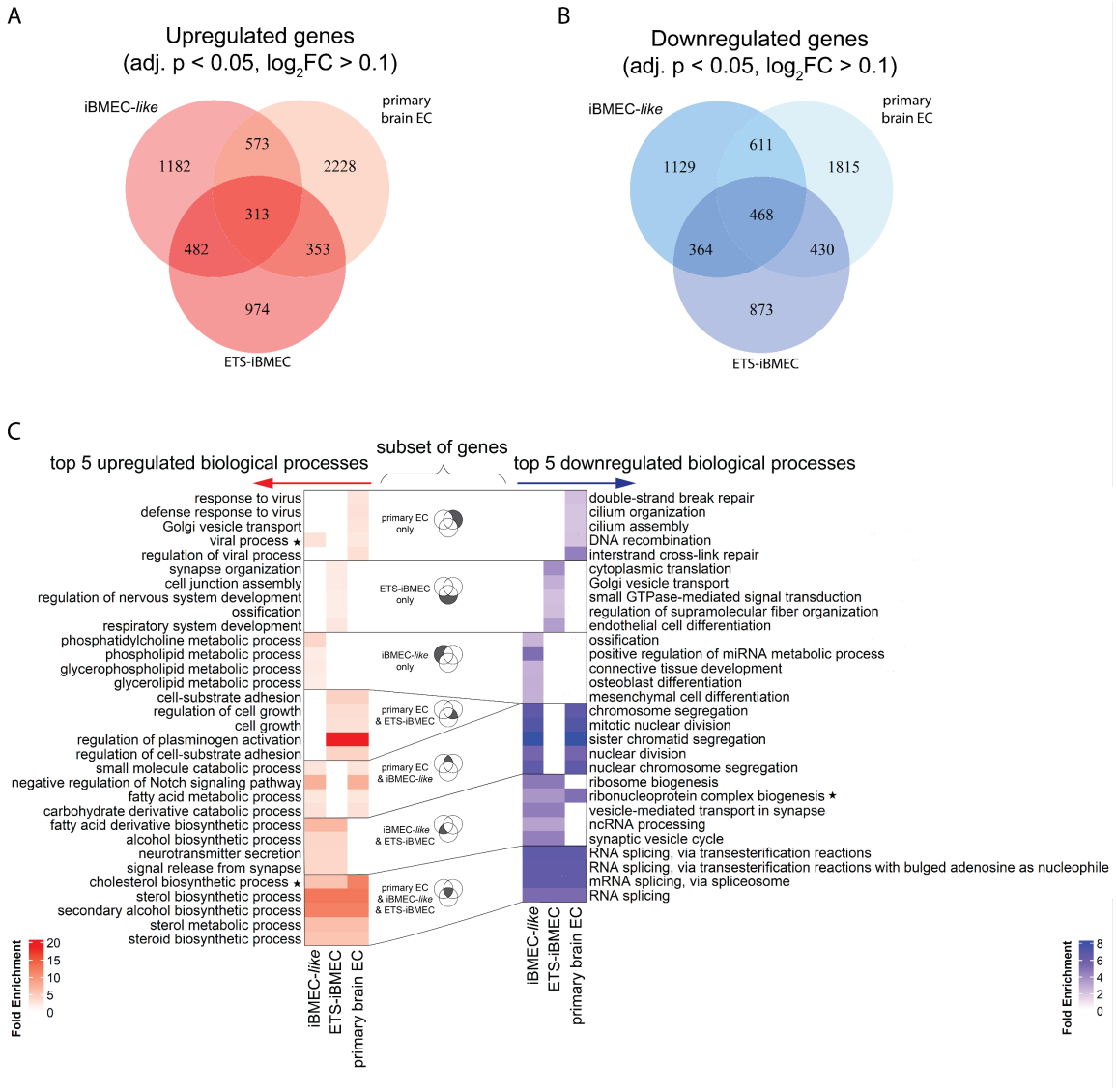

Fig. S5 – Differential gene expression in iBMEC-*like* cells, ETS-iBMEC and primary brain ECs after 24-hour malaria egress product exposure. Venn diagrams showing the overlap of significantly upregulated (**A**) and downregulated (**B**) genes (adjusted p value < 0.05, $\log_2$ fold change > ± 0.1) among the three cell types following exposure. (**C**) The top 5 enriched GO biological process terms for each subset of differentially expressed genes identified in the Venn diagrams. Heatmaps show fold enrichment of each GO term for the relevant cell-type-specific or shared gene subsets. Star indicates GO term expression in another Venn diagram subset.

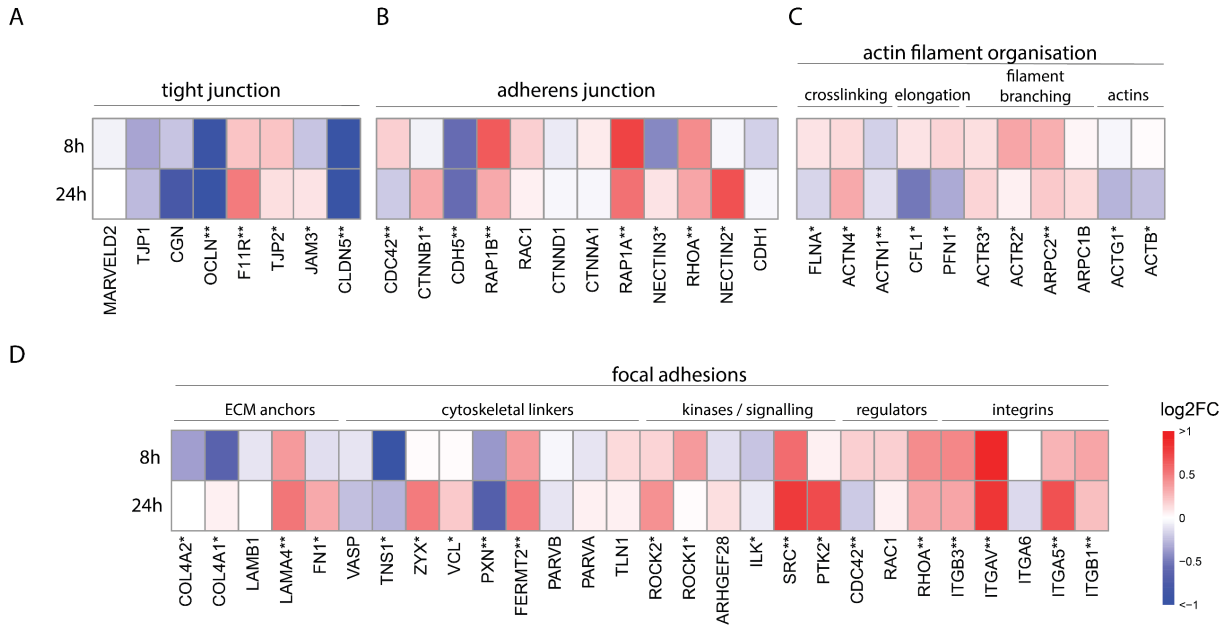

Fig. S6 – Transcriptional response of primary brain ECs to malaria egress products. Heatmaps show $\log_2$ fold changes in key genes related to tight junctions (**A**), adherens junctions (**B**), actin filaments (**C**), and focal adhesions (**D**) after 8- and 24-hour egress product exposure versus controls. Asterisks denote significant DESeq2 differential expression (adjust. p-value <0.05) at one (*) or both (**) time points.